

JET FORMATION IN BLACK HOLE ACCRETION SYSTEMS II: NUMERICAL MODELS

JONATHAN C. MCKINNEY¹

June 16, 2005

ABSTRACT

In a companion theory paper, we presented a unified model of jet formation. We suggested that primarily two types of relativistic jets form near accreting black holes: a potentially ultrarelativistic Poynting-dominated jet and a Poynting-baryon jet. We showed that, for the collapsar model, the neutrino-driven enthalpy flux (classic fireball model) is probably dominated by the Blandford-Znajek energy flux, which predicts a jet Lorentz factor of $\Gamma \sim 100 - 1000$. We showed that radiatively inefficient AGN, such as M87, are synchrotron-cooling limited to $\Gamma \sim 2 - 10$. Radiatively efficient x-ray binaries, such as GRS1915+105, are Compton-drag limited to $\Gamma \lesssim 2$, but the jet may be destroyed by Compton drag. However, the Poynting-baryon jet is a collimated outflow with $\Gamma \sim 1 - 3$. Here we present general relativistic hydromagnetic simulations of black hole accretion with pair creation used to simulate jet formation in GRBs, AGN, and x-ray binaries. Our collapsar model shows the development of a patchy “magnetic fireball” with typically $\Gamma \sim 100 - 1000$ and a Gaussian structure. Temporal variability of the jet is dominated by toroidal field instabilities for $\gtrsim 10^2$ gravitational radii. A broader Poynting-baryon jet with $\Gamma \sim 1.5$ could contribute to a supernova.

Subject headings: accretion disks, black hole physics, galaxies: jets, gamma rays: bursts, X-rays : bursts, supernovae: general, neutrinos

1. INTRODUCTION

General relativistic magnetohydrodynamics (GRMHD) is the black hole mass-invariant (nonradiative) physics commonly used to describe black hole accretion systems. Such systems often exhibit jets. However, the observed jet properties, such as collimation and speed, are not uniform between systems. In McKinney (2005b), our goal was to determine the unifying, or minimum number of, pieces of physics that would explain jet formation associated with gamma-ray bursts (GRBs), active galactic nuclei (AGN), and x-ray binaries. Similar ideas have been explored by other authors (Ghisellini & Celotti 2002; Ghisellini 2003; Meier 2003). The goal of McKinney (2005b) was to understand jet *formation* and explain the origin of the energy, composition, collimation, and Lorentz factor.

This paper implements some of the theoretical ideas of McKinney (2005b) into a GRMHD numerical model. In particular, we study the collapsar model with pair creation and an effective model for Fick diffusion of neutrons that contaminate the jet with an electron-proton plasma. The generic model parameters also allow the numerical model to be interpreted as a model for AGN systems such as M87. We also comment on the applicability of the model to x-ray binary systems.

§ 2 summarizes the proposed unified model to explain jet formation in all black hole accretion systems, where more details are provided in McKinney (2005b).

§ 3 presents the results of a fiducial numerical model corresponding to the collapsar model and describes the jet structure and formation. The relevance of the presented model to AGN and x-ray binaries is discussed. The jet is found to have some piece-wise self-similar features, and curve fits are given for use by other modellers. Acceleration of the GRB jet is found to occur over a large range in radii rather than occurring close

to the black hole. The introductory estimates of the Lorentz factor in McKinney (2005b) are refined based upon these numerical models. The jet characteristic structure, such as the formation of a double transonic (transfast) flow, is discussed.

§ 4 discusses the results and their possible implications. The results are compared to similar investigations, and the limitations of the models presented are discussed.

§ 5 summarizes the key points.

In appendix A, we give the GRMHD equations of motion solved when accounting for pair creation. See also McKinney (2005b) for relevant discussions. These are the equations numerically solved that give the results discussed in section 3. These are straightforward and how one handles the details of the pair creation ends up not making any qualitative (or much quantitative) difference in the results, hence why the material is in the appendix. That is, the energetics of the Poynting-dominated jet are dominated by the electromagnetic field. Appendix B summarizes the well-known characteristics of the GRMHD equations and other surfaces of physical interest used in the discussion in section 3.

2. GRMHD PAIR INJECTION MODEL OF JET FORMATION

In McKinney (2005b), we showed that one can identify a small subset of physics that can explain the jet energy, composition, collimation, and Lorentz factor for all black hole accretion systems.

One key idea of that paper is that the terminal Lorentz factor is determined by the toroidal magnetic energy per unit pair mass density energy near the location where pairs can escape to infinity (beyond the so-called “stagnation surface”). For GRBs, neutron diffusion is crucial to explain (and limit) the Lorentz factor and explain the baryon-pollution or baryon-contamination problem. For AGN and x-ray binaries, since a negligible number of baryons cross the field lines, pair-loading from radiative annihilation is crucial to determine the Lorentz factor of the Poynting-dominated jet since this determines the rest-mass flux and density in the jet.

Figure 1 shows the basic picture for GRB systems, while figure 2 shows the basic picture for AGN and x-ray binary

¹ Institute for Theory and Computation, Harvard-Smithsonian Center for Astrophysics, 60 Garden Street, MS 51, Cambridge, MA 02138, USA

High Res. Figures: <http://rainman.astro.uiuc.edu/~jon/jet2.pdf>
 Electronic address: jmcKinney@cfa.harvard.edu

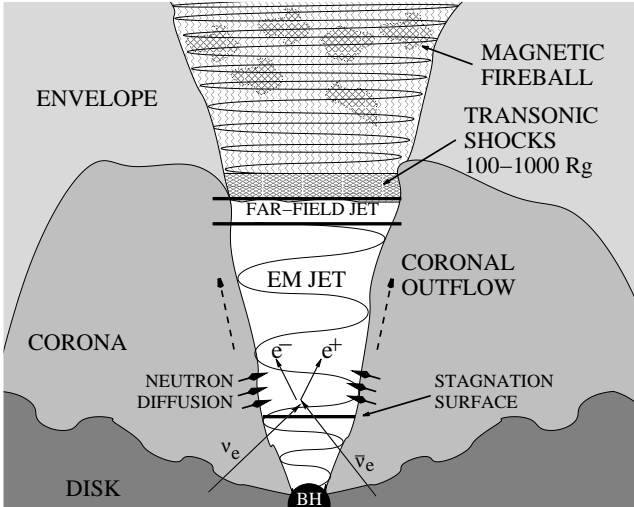


FIG. 1.— Schematic of pair-production model and subsequent magnetic fireball formation for GRB disks. Fireball is extremely optically thick. Below a stagnation surface, pairs are accreted by the black hole and so do not load the jet. Here $Rg = GM/c^2$.

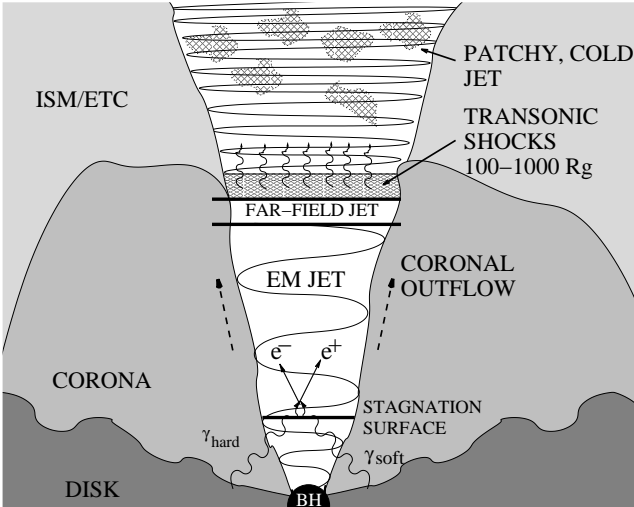


FIG. 2.— Schematic of pair-production model and subsequent shock-heating and emission. AGN jet is optically thin and emits nonthermal and thermal synchrotron, while x-ray binary jet can be marginally optically thick and emit via self-absorbed synchrotron and by severe Compton drag. Severe Compton drag can lead to destruction of the Poynting-dominated jet.

systems. An accreting, spinning black hole creates a magnetically dominated funnel region around the polar axis. The rotating black hole drives a Poynting flux into the funnel region, where the Poynting flux is associated with the coiling of poloidal magnetic field lines into toroidal magnetic field lines. The ideal MHD approximation holds very well, and so only neutral particles such as photons, neutrinos, and neutrons can cross the field lines and load the Poynting-dominated jet that emerges.

The accretion disk emits neutrinos in a GRB model (γ -ray and many soft photons for AGN and x-ray binaries) that annihilate and pair-load the funnel region within some “injection region.” For GRB systems, neutrons Fick-diffuse across the field lines and collisionally decay into an electron-proton plasma.

Many pairs (any type) are swallowed by the black hole, but some escape if beyond some “stagnation surface,” where the time-averaged poloidal velocity is zero and positive beyond.

Pairs beyond the stagnation surface are then accelerated by the Poynting flux in a self-consistently generated collimated outflow. In the electromagnetic (EM) jet, the acceleration process corresponds to a gradual uncoiling of the magnetic field and a release of the stored magnetic energy that originated from the spin energy of the black hole.

One key result of this paper is that the release of magnetic energy need not be gradual once the toroidal field dominates the poloidal field, in which case pinch (and perhaps kink) instabilities can occur and lead to a nonlinear coupling (e.g. a shock) that converts Poynting flux into enthalpy flux (Eichler 1993; Begelman 1998). In the proposed GRB model, this conversion reaches equipartition and the jet becomes a “magnetic fireball,” where the toroidal field instabilities drive large variations in the jet Lorentz factor and jet luminosity.

In McKinney (2005b), we showed that in AGN systems, nonthermal synchrotron from shock-accelerated electrons and some thermal synchrotron emission releases the shock energy until the synchrotron cooling times are longer than the jet propagation time. For AGN, jet acceleration is negligible beyond the *extended* shock zone, as suggested for blazars beyond the “blazar zone” (Sikora et al. 2005). In x-ray binary systems, the shock is not as hot and also unlike in the AGN (at least those like M87) case the jet can be optically thick. Thus these x-ray binary systems self-absorbed synchrotron emit if they survive Compton drag.

For all these systems, at large radii patches of energy flux and variations in the Lorentz factor develop due to toroidal instabilities. These patches in the jet could drive internal shocks and at large radii they drive external shocks with the surrounding medium. The EM jet is also surrounded by a mildly relativistic matter coronal outflow/jet/wind, which is a material extension of the corona surrounding the disk. This Poynting-baryon, coronal outflow collimates the outer edge of the Poynting-dominated jet, which otherwise internally collimates by hoop stresses. The luminosity of the Poynting-baryon jet is determined, like the Poynting-dominated jet, by the mass accretion rate, disk thickness, and black hole spin.

In this paper, this unified model is studied numerically using axisymmetric, nonradiative, GRMHD simulations to study the self-consistent process of jet formation from black hole accretion systems. These simulations extend the work of McKinney & Gammie (2004) by including pair creation (and an effective neutron diffusion for GRB-type systems) to self-consistently treat the creation of jet matter, investigating a larger dynamic range in radius, and presenting a more detailed analysis of the Poynting-dominated jet structure.

2.1. Units and Notation

The units in this paper have $GM = c = 1$, which sets the scale of length ($r_g \equiv GM/c^2$) and time ($t_g \equiv GM/c^3$). The mass scale is determined by setting the (model-dependent) observed (or inferred for GRB-type systems) mass accretion rate ($\dot{M}_0 [g s^{-1}]$) equal to the accretion rate through the black hole horizon as measured in a simulation. So the mass is scaled by the mass accretion rate (\dot{M}_0) at the horizon ($r = r_H \equiv r_L(1 + \sqrt{1 - j^2})$), such that $\rho_{0,disk} \equiv \dot{M}_0[r = r_H]t_g/r_g^3$ and the mass scale is then just $m \equiv \rho_{0,disk}r_g^3 = \dot{M}_0[r = r_H]t_g$. Unless explicitly stated, the magnetic field strength is given in Heaviside-Lorentz units, where the Gaussian unit value is obtained by multiplying the Heaviside-Lorentz value by $\sqrt{4\pi}$.

The value of $\rho_{0,disk}$ can be determined for different systems. For example, a collapsar model with $\dot{M} = 0.1 M_\odot s^{-1}$ and

$M \approx 3M_{\odot}$, then $\rho_{0,disk} \approx 3.4 \times 10^{10} \text{ g cm}^{-3}$. M87 has a mass accretion rate of $\dot{M} \sim 10^{-2} M_{\odot} \text{ yr}^{-1}$ and a black hole mass of $M \approx 3 \times 10^9 M_{\odot}$ (Ho 1999; Reynolds et al. 1996) giving $\rho_{0,disk} \sim 10^{-16} \text{ g cm}^{-3}$. GRS 1915+105 has a mass accretion rate of $\dot{M} \sim 7 \times 10^{-7} M_{\odot} \text{ yr}^{-1}$ (Mirabel & Rodriguez 1994; Mirabel & Rodríguez 1999; Fender & Belloni 2004) with a mass of $M \sim 14 M_{\odot}$ (Greiner et al. 2001), but see Kaiser et al. (2004). This gives $\rho_{0,disk} \sim 3 \times 10^{-4} \text{ g cm}^{-3}$. This disk density scales many of the results of the paper. The disk height (H) to radius (R) ratio is written as H/R .

The GRMHD notation follows MTW. For example, the 4-velocity components are u^{μ} (contravariant) or u_{μ} (covariant). For a black hole with angular momentum $J = jGM^2/c$, $j/a/M$ is the dimensionless Kerr parameter with $-1 \leq j \leq 1$. The rest-mass density is given as ρ_0 , internal energy density as u , magnetic field 3-vector as $B^i \equiv {}^*F^{ii}$, where *F is the dual of the Faraday tensor. The contravariant metric components are $g^{\mu\nu}$ and covariant components are $g_{\mu\nu}$, where beyond the frame-dragging of the black hole the metric in Boyer-Lindquist coordinates is approximately diagonal such that an orthonormal contravariant component is $u^{\hat{\mu}} = \sqrt{g_{\mu\mu}} u^{\mu}$ for any spatial component of u^{μ} . The comoving energy density is $b^2/2$, where b^{μ} is the comoving magnetic field. See McKinney & Gammie (2004) for details.

The Lorentz factor of the jet can be measured either as the current time-dependent value, or, using information about the GRMHD system of equations, one can estimate the Lorentz factor at large radii from fluid quantities at small radii. The Lorentz factor as measured by a static observer at infinity is

$$\Gamma \equiv u^{\hat{t}} = u^t \sqrt{-g_{tt}} \quad (1)$$

in Boyer-Lindquist coordinates, where no static observers exist inside the ergosphere. This is as opposed to $W \equiv u^t \sqrt{-1/g^{tt}}$, which is the Lorentz factor as measured by the normal observer as used by most numerical relativists.

In McKinney (2005b) we show that the Lorentz factor and ϕ -velocity at large distances are

$$\Gamma_{\infty} = E = -hu_t + \Phi\Omega_F B_{\phi} \quad (2)$$

$$u_{\infty}^{\hat{\phi}} = L = hu_{\phi} + \Phi B_{\phi}, \quad (3)$$

where $h = (\rho_0 + u_g + p)/\rho_0$ is the specific enthalpy, Φ is the conserved magnetic flux per unit rest-mass flux, Ω_F is the conserved field rotation frequency, B_{ϕ} is the covariant toroidal magnetic field, and $u_{\infty}^{\hat{\phi}} = u_{\phi,\infty}$. Here E and L simply represent the conserved energy and angular momentum flux per unit rest-mass flux. Notice the matter and electromagnetic pieces are separable, such that

$$\Gamma_{\infty} = \Gamma_{\infty}^{(MA)} + \Gamma_{\infty}^{(EM)} \quad (4)$$

$$u_{\phi,\infty} = u_{\phi,\infty}^{(MA)} + u_{\phi,\infty}^{(EM)}, \quad (5)$$

See McKinney (2005b) for more details.

3. NUMERICAL EXPERIMENTS

This section presents the results of GRMHD numerical models with pair creation to self-consistently describe the Poynting-dominated and Poynting-baryon jet formation process. Our numerical scheme is HARM (Gammie et al. 2003a), a conservative, shock-capturing scheme for evolving the equations of general relativistic MHD. Compared to the original HARM, the inversion of conserved quantities to primitive variables is performed by using a new faster and

more robust two-dimensional non-linear solver (Noble et al. 2005). The new HARM also uses a parabolic interpolation scheme (Colella 1984) rather than a linear interpolation scheme. The new HARM also uses an optimal TVD third order Runge-Kutta time stepping (Shu 1997) rather than the mid-point method. For the problems under consideration, the parabolic interpolation and third order time stepping method reduce the truncation error significantly, including magnetically dominated regions with $b^2/\rho_0 \gg 1$.

Notice that no explicit reconnection model is included. However, HARM checks the effective resistivity by measuring the rest-mass flux across field lines. For the boundary between the coronal wind and the Poynting-dominated jet, the total mass flux across the field line is negligible compared to the rest-mass flux along the field line and the pair creation rate. An unresolved model would load field lines with rest-mass that crosses field lines and not properly represent any physical resistivity (McKinney 2004).

3.1. Computational Domain

The computational domain is *axisymmetric*, with a grid that typically extends from $r_{in} = 0.98r_H$, where r_H is the horizon, to $r_{out} = 10^4 r_g$, and from $\theta = 0$ to $\theta = \pi$. Full 3D calculations with this dynamic range are not possible with today's computers. Our numerical integrations are carried out on a uniform grid in so-called "modified KS" (MKS) coordinates: x_0, x_1, x_2, x_3 , where $x_0 = t[\text{KS}]$, $x_3 = \phi[\text{KS}]$. The radial coordinate is chosen to be

$$r = R_0 + e^{x_1^{n_r}}, \quad (6)$$

where R_0 is chosen to concentrate the grid zones toward the event horizon (as R_0 is increased from 0 to r_H) and n_r is controls the enhancement of inner to outer radial regions. For studies where the disk and jet interaction is of primary interest, $R_0 = 0$ and $n_r = 1$ are chosen. For studies where in addition the far-field jet is of interest, $R_0 = -3$ and $n_r = 10$ are chosen. The θ coordinate is chosen to be

$$\theta = \pi x_2 + \frac{1}{2}(1 - h(r)) \sin(2\pi x_2), \quad (7)$$

where $h(r)$ is used to concentrate grid zones toward the equator (as h is decreased from 1 to 0) or pole (as h is increased from 1 to 2). The jet at large radii is resolved together with the disk at small radii using

$$h(r) = 2 - Q_j(r/r_{0j})^{-n_j g_j} \quad (8)$$

with the parameters of $Q_j = 1.3 - 1.8$, $r_{0j} = 2.8$, $n_j = 0.3$, $r_{1j} = 20$, $r_{2j} = 80$, and $g_j = g_j(r) = \frac{1}{2} + \frac{1}{\pi} \text{atan}(\frac{r-r_{2j}}{r_{1j}})$ is used to control the transition between inner and outer radial regions. To perform convergence tests, Q_j and the overall radial and θ resolution are varied. An alternative to this fixed refinement of the jet and disk is an adaptive refinement (see, e.g., Zhang & MacFadyen 2005).

3.2. Initial Conditions and Problem Setup

All the experiments evolve a weakly magnetized torus around a Kerr black hole in axisymmetry. The focus of our numerical investigation is to study a high resolution model of the collapsar model. Other simulations were performed, and the fiducial model's relevance to AGN and x-ray binary systems is discussed at the end of the section. A generic model is used so the results mostly can be applied to any black hole system. A black hole spin of $j = 0.9375$ is chosen, but this

produces similar results to models with $0.5 \lesssim j \lesssim 0.97$, which includes most black hole accretion systems.

The initial conditions consist of an equilibrium torus which is a “donut” of plasma with a black hole at the center (Fishbone & Moncrief 1976; Abramowicz, Jaroszinski, & Sikora 1978). The donut is supported against gravity by centrifugal and pressure forces. The solutions of Fishbone & Moncrief (1976) corresponding to $u^t u_\phi = \text{const.}$ are used. The initial inner edge of the torus is set at $r_{\text{edge}} = 6$. The equation of state is a gamma-law ideal gas with $\gamma = 4/3$, but other γ lead to similar results (McKinney & Gammie 2004). This donut is a solution to the axisymmetric stationary equations, but the donut is unstable to global nonaxisymmetric modes (Papaloizou & Pringle 1983). However, when the donut is embedded in a weak magnetic field, the magnetorotational instability (MRI) dominates those hydrodynamic modes. Small perturbations are introduced in the velocity field to seed the instability. The models have $u^t u_\phi = 4.281$, the pressure maximum is located at $r_{\text{max}} = 12$, the inner edge at $(r, \theta) = (6, \pi/2)$, and the outer edge at $(r, \theta) = (42, \pi/2)$.

This is consistent with the accretion disk that is expected to form in the collapsar model (MacFadyen & Woosley 1999). A GRB in the collapsar model is formed after the collapse of a massive star as a black hole with $M_{\text{BH}} \sim 3M_\odot$ and spin $j \sim 0.75 - 0.94$ accretes at $\dot{M}_0 \sim 0.1M_\odot/\text{s}$ from a torus of matter within $r < 200\text{ km}$ that has a height (H) to radius (R) ratio (“thickness”) of $H/R \sim 0.2 - 0.4$. MacFadyen & Woosley (1999) find that an energetic outflow develops in the polar region where $\rho \sim 10^7 \text{ g cm}^{-3}$ near the horizon, $\rho \sim 10^5 \text{ g cm}^{-3}$ at $r \sim 200\text{ km}$, and $\rho \sim 10^{3-4} \text{ g cm}^{-3}$ at $r \sim 2000\text{ km}$ (see model 14A in MacFadyen & Woosley 1999). In the parlance of collapsar models, our $u^t u_\phi$ model corresponds to a $j_{16} \equiv j/(10^{16} \text{ cm}^2 \text{s}^{-1})$ of $j_{16} \sim 5$, within the range suggested by MacFadyen & Woosley (1999) to produce a GRB. Also, the $H/R \sim 0.2 - 0.4$ as suggested that forms according to neutrino emission models (Kohri & Mineshige 2002; Kohri et al. 2005).

For radiatively inefficient AGN and x-ray binaries this is simply a reasonable approximate model for the inner-radial accretion flow. While a slightly thicker disk ($H/R \sim 0.9$) may be more appropriate for radiatively inefficient flows, this is not expected to significantly affect these results. A study of the effect of disk thickness, especially thin disks, is left for future work.

The orbital period at the pressure maximum $2\pi(a + (r_{\text{max}}/r_g)^{3/2})t_g \simeq 267t_g$, as measured by an observer at infinity. The model is run for $\Delta t = 1.4 \times 10^4 t_g$, which is about 52 orbital periods at the pressure maximum and about 1150 orbital periods at the black hole horizon. For the collapsar model this is only ~ 0.2 seconds, and at the spin chosen would correspond to the late phase of accretion when the Poynting flux reaches its largest magnitude. For the AGN M87 this corresponds to ~ 7 years. For the x-ray binary GRS 1915+105 this corresponds to ~ 1 second.

Notice that since the model is axisymmetric, disk turbulence is not sustained after about $t \sim 3000t_g$; that is, the anti-dynamo theorem prevails (Cowling 1934). However, while this affects the disk accretion, this does not affect the evolution of the Poynting-dominated jet. That is, from the time of turbulent accretion to “laminar” accretion, the funnel region is mostly unchanged. Indeed, the far-field jet that has already formed is causally disconnected from the region where the

accretion disk would still be turbulent.

For the collapsar model, at the quasi-steady state mass accretion rate of $0.1M_\odot/\text{s}$ the disk will last for $t \lesssim 0.42\text{s}$. Thus, this model requires a more extended disk or a fresh supply of plasma into the disk from the surrounding stellar envelope through an “accretion shock” to generate a long duration GRBs (MacFadyen & Woosley 1999). However, since any such system modelled is in quasi-steady state, the results here do not strongly depend on the mass of the disk as long as the disk is not too massive, which would require taking into account the self-gravity of the disk.

The numerical resolution of these models is 512×256 compared to 456^2 in McKinney & Gammie (2004). However, due to the enhanced θ grid, the resolution in the far-field jet region is ~ 10 times larger. Also, with the use of a parabolic interpolation scheme, the overall resolution is additionally enhanced. Compared to our previous model this gives us an effective θ resolution of ≈ 9000 .

As with McKinney & Gammie (2004), into the initial torus is put a purely poloidal magnetic field. The field can be described using a vector potential with a single nonzero component $A_\phi \propto \text{MAX}(\rho_0/\rho_{0,\text{max}} - 0.2, 0)$. The field is therefore restricted to regions with $\rho_0/\rho_{0,\text{max}} > 0.2$. The field is normalized so that the minimum ratio of gas to magnetic pressure is 100. The equilibrium is therefore only weakly perturbed by the magnetic field. It is, however, no longer stable (Balbus & Hawley 1991; Gammie 2004). Hirose et al. (2004); McKinney & Gammie (2004) show that no initial large-scale net vertical field is necessary, since a large-scale poloidal field is self-consistently generated. The field connects the black hole horizon (as observed by a physical observer) to large distances. Apart from the existence of an overall poloidal sign, the results are insensitive to the details of the initial magnetic field geometry for any physically motivated geometry (McKinney & Gammie 2004).

3.3. Floor vs. Pair Creation Model

Numerical models often “model” the injection physics in the Poynting-dominated jet by employing a so-called floor model. This model forces a minimum on the rest-mass density (ρ_{fl}) and internal energy density (u_{fl}), which are usually set to several orders of magnitude lower than the disk density. Actually, however, floor models have always been treated as a purely numerical invention in order to avoid numerical artifacts associated with the inability to numerically solve the equations of motion when the density is low. Indeed, the idea was one should convergence test by gradually lowering ρ_{fl} and u_{fl} . This is perhaps a reasonable for numerical study of stars, but accretion flows are so hot (baryons with $T \gtrsim 10^{10} \text{ K}$ in the thick disk state near the black hole) that pairs are created when neutrinos annihilate (or when photons annihilate for x-ray binary and AGN systems).

In previous numerical models of Poynting jets, the funnel region is always completely evacuated, and floor-models necessarily generate mass at least where the poloidal velocity $u^p = 0$ at the stagnation surface. That is, matter inside the stagnation surface falls into the black hole, while matter outside it is ejected as part of the jet. Indeed, arbitrary floor-models violate the ideal-MHD condition far away from the black hole where no pairs should be produced. For example, if a numerical model uses $\rho_{\text{fl}} \sim \text{Const.}$, then this leads to a completely unphysical model of pair creation and the ideal-MHD approximation is violated for the entire length of the jet in the funnel.

While pair creation has so far been ignored by those doing

numerical models of jets from black hole accretion systems, it has been shown that the properties of the Poynting-dominated jet are almost completely determined by the pair creation physics, which thus cannot be ignored (Phinney 1983; Punsly 1991; Levinson 2005).

Our collapsar model accounts for pair creation and Fick diffusion of neutrons. In this paper, there is an injected rest-mass, enthalpy, and momentum. For the fiducial collapsar-like model, rest-mass, enthalpy, and momentum are injected with energy at infinity fractions of, respectively, $f_p = 0.05$, $f_h = 0.45$, and $f_m = 0.5$ as described in McKinney (2005b). The total energy at infinity injected is determined by neutrino annihilation rates and Fick diffusion rates. The energy injection rate from neutrino annihilation is based upon viscous disk models (Popham et al. 1999; MacFadyen & Woosley 1999), where the rate of injection is determined by choosing a viscosity coefficient $\alpha = 0.01$ and mass accretion rate $\dot{M}_0 = 0.1 M_{\odot} s^{-1}$ for the collapsar model. As discussed in that paper, the rest-mass is dominated by electron-positron pairs only very close to the black hole.

The value of α and \dot{M}_0 determine the energy injected in proportion to the disk density per unit light crossing time (t_g). Thus any system with comparable normalized energy injection rate would follow similar results. For example, the M87 model is similar, where there the electron-positron pairs do not annihilate and represent the true density in the jet. In the M87 model there is no Fick diffusion, yet the dimensionless model parameters are approximately the same.

The momentum direction is chosen by setting $u_{inj}^{\phi} = u^{\phi}$ and $u_{inj}^{\theta} = 0$, so that f_m determines u^r_{inj} . It turns out that the choice of f_h , f_m , and the injected momentum direction very weakly determine the jet structure for $r \gtrsim 6r_g$. This is because a large fraction of the pairs are lost to the black hole and magnetic forces, rather than the injected momentum, dominate the motion of the plasma near the black hole.

Beyond this injection region, the rest-mass is dominated by electron-protons created in collision events from neutrons that Fick diffuse across the field lines into the jet region. For the collapsar model this coincidentally corresponds to the injected rest-mass injected in this model. Since the electron-positron pair annihilation only gives an additional $\sim 10\%$ of internal energy, then pair annihilation need not be considered, and the rest-mass injected well-models the rest-mass injected as an electron-proton plasma from Fick-diffused neutrons that collisionally decay.

This physical model of the injected particles is augmented when the rest-mass or internal energy density reaches very low values. If the density drops below some “floor” value, then the density is returned to the floor value. The floor model chosen has $\rho_{fl} = 10^{-7} r^{-2.7} \rho_{0,disk}$ and $u_{fl} = 10^{-9} r^{-2.7} \rho_{0,disk}$. HARM keeps track of how often the density goes below the floors and how this modifies the conservation of mass, energy, and angular momentum. The floor model contribution is negligible compared to the physical injection model at all spatial locations and at all times. The coefficient of the floor was chosen to be close to the resulting density near the black hole horizon. It was not chosen arbitrarily small in order to avoid numerical difficulties in integrating the equations when, rarely, the floor is activated in regions of large magnetic energy density per unit rest-mass density.

3.4. Boundary Conditions

Two different models are chosen for the outer boundary condition. One model is called an “outflow” boundary condition, for which all primitive variables are projected into the ghost zones while forbidding inflow. The other model is to inject matter at some specified rate at the outer boundary, unless there is outflow. This would correspond to a Bondi-like infall for AGN and x-ray binaries, or would correspond to the collapsing envelope of a massive star for collapsar models. In particular, unless there is outflow, the outer boundary is set to inject mass at the free-fall rate, with a density of $\rho_0 = 10^{-4} r^{-3/2} \rho_{0,disk}$ and $u = 10^{-6} r^{-5/2} \rho_{0,disk}$ and no angular momentum. Presupernova models suggest that the infalling matter is at about 30% the free-fall rate we have chosen above (MacFadyen & Woosley 1999), but this difference is unlikely to significantly affect the jet formation. Also, for their collapsar model, the density structure in the equatorial plane varies between $\rho_0 \propto r^{-3/2}$ to $\rho_0 \propto r^{-2}$ and the internal energy is $u \propto r^{-5/2}$ to $u \propto r^{-2.7}$ (MacFadyen & Woosley 1999). This is similar to our simplified model, which happens to also model a Bondi accretion for AGN and x-ray binaries. Thus the results are indicative of GRBs, AGN, and x-ray binaries. The outer grid radius corresponds to about 20 presupernova core radii (Woosley & Weaver 1995) or $\sim 10^{10}$ km or about 1/10th the entire star’s radius.

3.5. Fiducial Model

The overall character of the accretion flow is unchanged compared to the descriptions given in McKinney & Gammie (2004). The disk enters a long, quasi-steady phase in which the accretion rates of rest-mass, angular momentum, and energy onto the black hole fluctuate around a well-defined mean. Meanwhile, as in McKinney & Gammie (2004), a Poynting-dominated jet and Poynting-baryon jet (coronal outflow) have formed. The Poynting-dominated jet forms once the ram pressure of the funnel material is lower than the toroidal magnetic pressure. Afterwards the baryons are spread apart in the launch of a magnetic tube filled with pairs. This occurs within $t \lesssim 500 t_g$.

The Poynting-dominated jet forms as the differential rotation of the disk and the frame-dragging of the black hole induce a significant toroidal field that launches material away from the black hole by the same force described in McKinney (2005b).

A coronal outflow is also generated between the disk and Poynting-dominated jet. In this model the coronal outflow has $\Gamma_{\infty} \sim 1.5$. The coronal-funnel boundary contains shocks with a sonic Mach number of $M_s \sim 100$. The inner-radial interface between the disk and corona is a site of vigorous reconnection due to the magnetic buoyancy and convective instabilities present there. These two parts of the corona are about 100 times hotter than the bulk of the disk. Thus these coronal components are a likely sites for Comptonization and nonthermal particle acceleration.

Figure 3 and figure 4 show the final time ($t = 1.4 \times 10^4 t_g$) log of rest-mass density and magnetic field projected on the Cartesian z vs. x plane. For the purposes of properly visualizing the accretion flow and jet, we follow MacFadyen & Woosley (1999) and show both the negative and positive x -region by duplicating the axisymmetric result across the vertical axis. Color represents $\log(\rho_0 / \rho_{0,disk})$ with dark red highest and dark blue lowest. The final state has a density maximum of $\rho_0 \approx 2\rho_{0,disk}$ and a minimum of $\rho_0 \sim 10^{-13} \rho_{0,disk}$ at large radii. Grid zones are not smoothed

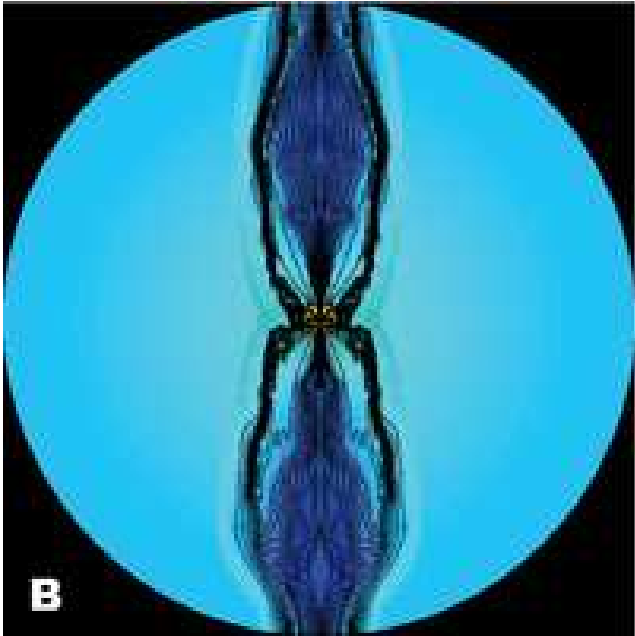
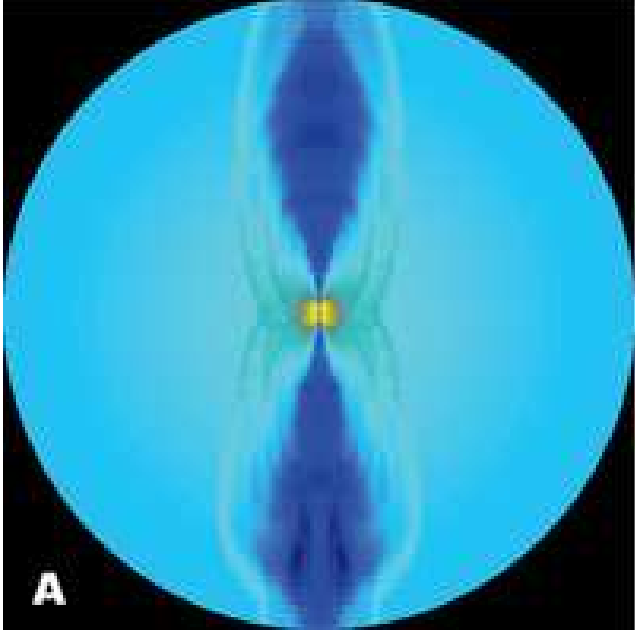


FIG. 3.— Jet has pummeled its way through presupernova core and through 1/10th of entire star. Time is $t = 1.4 \times 10^4 t_g$. Panel (A) shows final distribution of $\log \rho_0$ on the Cartesian plane. Black hole is located at center. Red is highest density and black is lowest. Panel (B) shows magnetic field overlaid on top of $\log \rho_0$. Outer scale is $r = 10^4 GM/c^2$.

to show grid structure. Outer radial zones are large, but outer θ zones are below the resolution of the figure.

Clearly the jet has pummeled its way through the surrounding medium, which corresponds to the stellar envelope in the collapsar model. By the end of the simulation, the field has been self-consistently launched into the funnel region and has a regular geometry there. In the disk and at the surface of the disk the field is curved on the scale of the disk scale height. Within $r \lesssim 10^2 r_g$ the funnel field is ordered and stable due to the poloidal field dominance. However, beyond

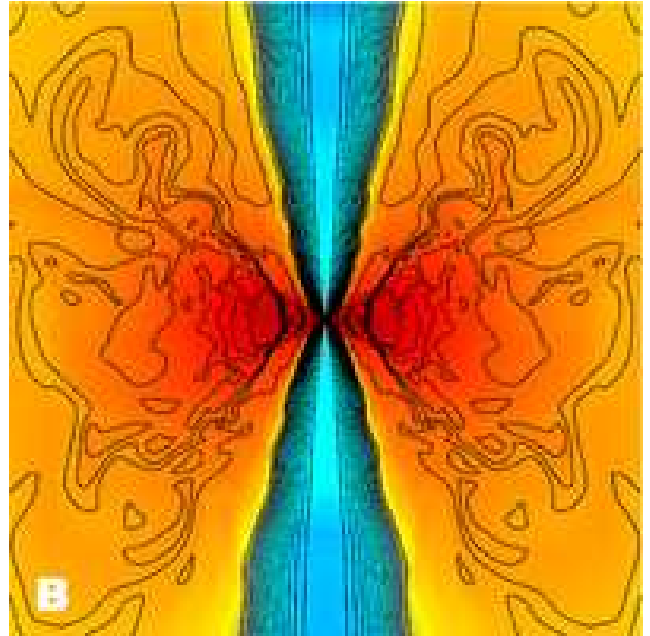
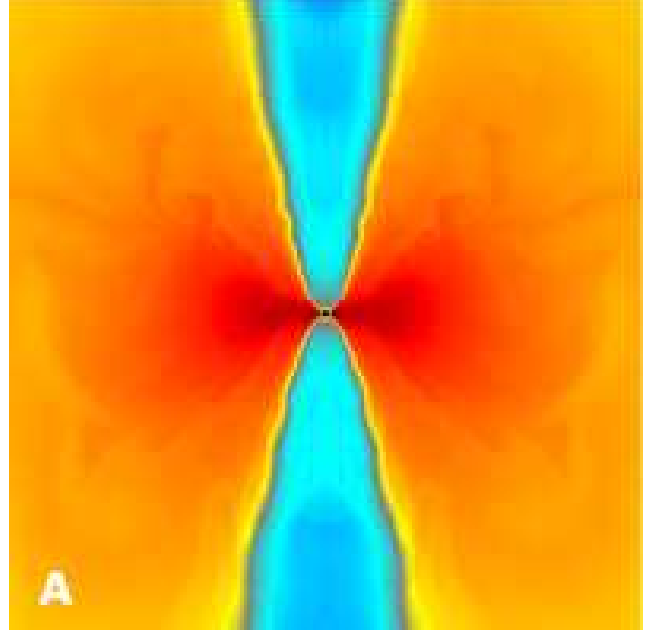


FIG. 4.— Strongest magnetic field near black hole in X-configuration due to Blandford-Znajek effect and collimation of disk+coronal outflow. As in figure 3, but outer scale is $r = 10^2 GM/c^2$. Time is $t = 1.4 \times 10^4 t_g$. Black hole is black circle at center. Color scale is same as in figure 3.

$r \sim 10 - 10^2 r_g$ the poloidal field is relatively weak compared to the toroidal field and the field lines bend and oscillate erratically due to pinch instabilities. The radial scale of the oscillations is $10^2 r_g$ (but up to $10^3 r_g$ and as small as $10 r_g$), where $r \sim 10 r_g$ is the radius where poloidal and toroidal field strengths are equal. By the end of the simulation, the jet has only fully evolved to a state independent of the initial conditions at $r \approx 5 \times 10^3 r_g$, beyond which the jet features are a result of the tail-end of the initial launch of the field. The head of the jet has passed beyond the outer boundary of $r = 10^4 r_g$. Notice that the magnetic field near the black hole

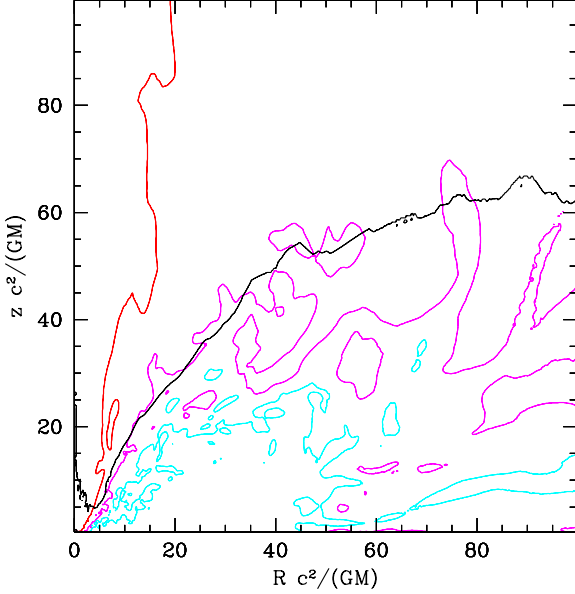


FIG. 5.— Contours for $t \approx 1500t_g$ and an outer scale of $r \approx 10^2r_g$, where the disk-corona boundary is a cyan contour where $\beta \approx u/b^2 = 3$, the coronal-wind boundary is a magenta contour where $\beta = 1$, and the jet-wind boundary is a red contour where $b^2/(\rho_0 c^2) = 1$. Black contour denotes boundary beyond which material is unbound and outbound (wind + jet). Beyond $r \approx 10r_g$ the jet undergoes poloidal oscillations due to a toroidal pinch instability.

is in an X-configuration. This is due to the BZ-effect having power $P_{jet} \propto \sin^2 \theta$, which vanishes at the polar axis. The X-configuration is also related to the fact that the disk+corona is collimating the Poynting-dominated jet. The field is mostly monopolar near the black hole, and such field geometries *decollimate* for rapidly rotating black holes in force-free electrodynamics (Krasnopol'sky et al. 2005).

Figures 5 and 6 show the energy structure of the disk, corona, and jet. This figure is comparable to the left panel of figure 2 in McKinney & Gammie (2004). Figure 5 shows contours for $t \approx 1500t_g$ and an outer scale of $r = 10^2r_g$, while figure 6 shows contours for $t \approx 1.4 \times 10^4t_g$ and an outer scale of $r = 10^3r_g$. The disk-coronal boundary is represented as a cyan contour where $\beta \equiv p_g/p_b \equiv 2(\gamma-1)u/b^2 = 3$, the coronal-wind boundary as a magenta contour where $\beta = 1$, and the jet-wind boundary as a red contour where $b^2/(\rho_0 c^2) = 1$. The black contour denotes the boundary beyond where material is unbound and outbound (wind or jet). Beyond $r \approx 10r_g$ the jet undergoes poloidal oscillations due to toroidal pinch instabilities, which subside by $r \approx 10^2 - 10^3r_g$ where the jet is thermally supported. At large scales, the cyan and magenta contours closer to the equatorial plane are not expected to cleanly distinguish any particular structure.

Figure 7 shows the disk, corona, and jet magnetic field structure during the turbulent phase of accretion at $t \approx 1500t_g$. Compared to figure 4, this shows the turbulence in the disk, but is otherwise similar. The jet, disk, and coronal structures remain mostly unchanged at late times despite the decay of disk turbulence. That is, the current sheets in the disk do not decay and continue to support the field around the black hole that leads to the Blandford-Znajek effect. The corona thickness and radial extent do not require the disk turbulence, which only adds to the time-dependence of the coronal outflow.

Figure 8 shows a color plot of Γ_∞ , where red is highest and

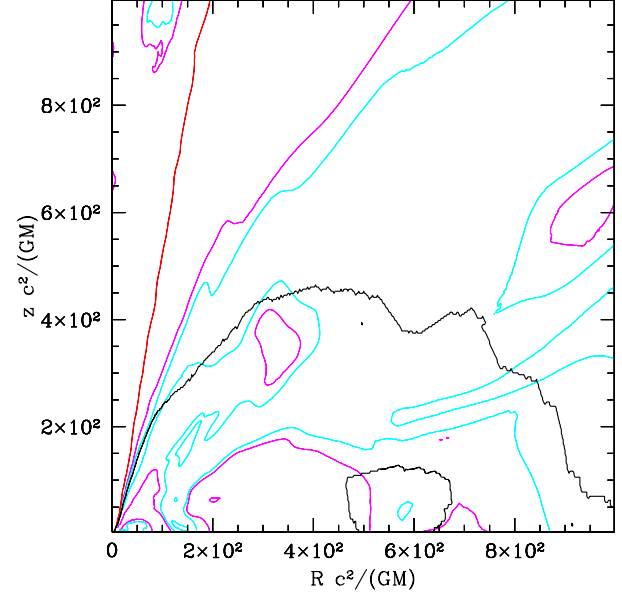


FIG. 6.— Same as figure 5 but for $t \approx 1.4 \times 10^4t_g$ and an outer scale of $r \approx 10^3r_g$. Disk wind leads to broad coronal outflow. Jet remains collimated to a fixed opening angle. By $r \gtrsim 100r_g$, pinch instabilities subside once magnetic energy converted into thermal energy and supports jet. Residual slow dense and fast diffuse patches from the instability are present in the jet, such as the slower and cooler dense blob shown at top left corner of figure.

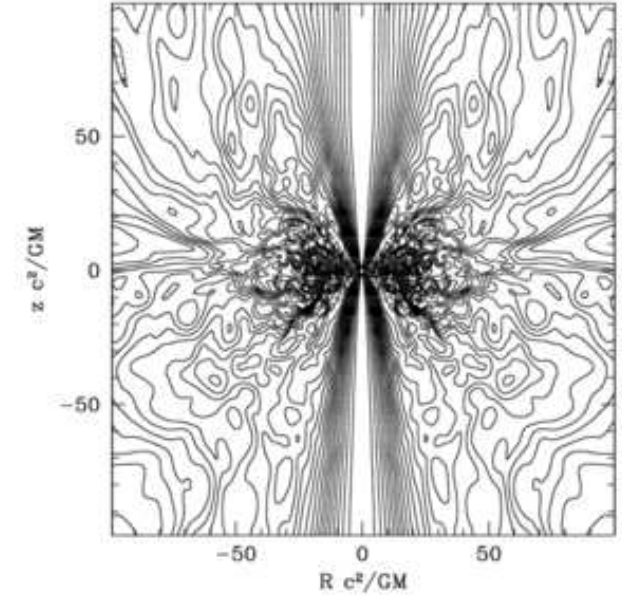


FIG. 7.— Field geometry near black hole for $t \approx 1500t_g$ during phase of strong disk turbulence.

reaches up to $\Gamma_\infty \sim 10^3 - 10^4$ and yellow has $\Gamma_\infty \sim 10^2 - 10^3$. Panel (A) shows outer scale of $r = 10^4r_g$, while panel (B) shows outer scale of $r = 10^3r_g$ with same color scale. The inner-radial region is not shown since Γ_∞ is divergent near injection region where ideal-MHD breaks down. Different realizations (random seed of perturbations in disk) lead to up to about $\Gamma_\infty \sim 10^4$ as shown for the lower pole in the color figures. This particular model was chosen for presentation for its diversity between the two polar axes. The upper polar axis is fairly well-structured, while the lower polar axis has under-

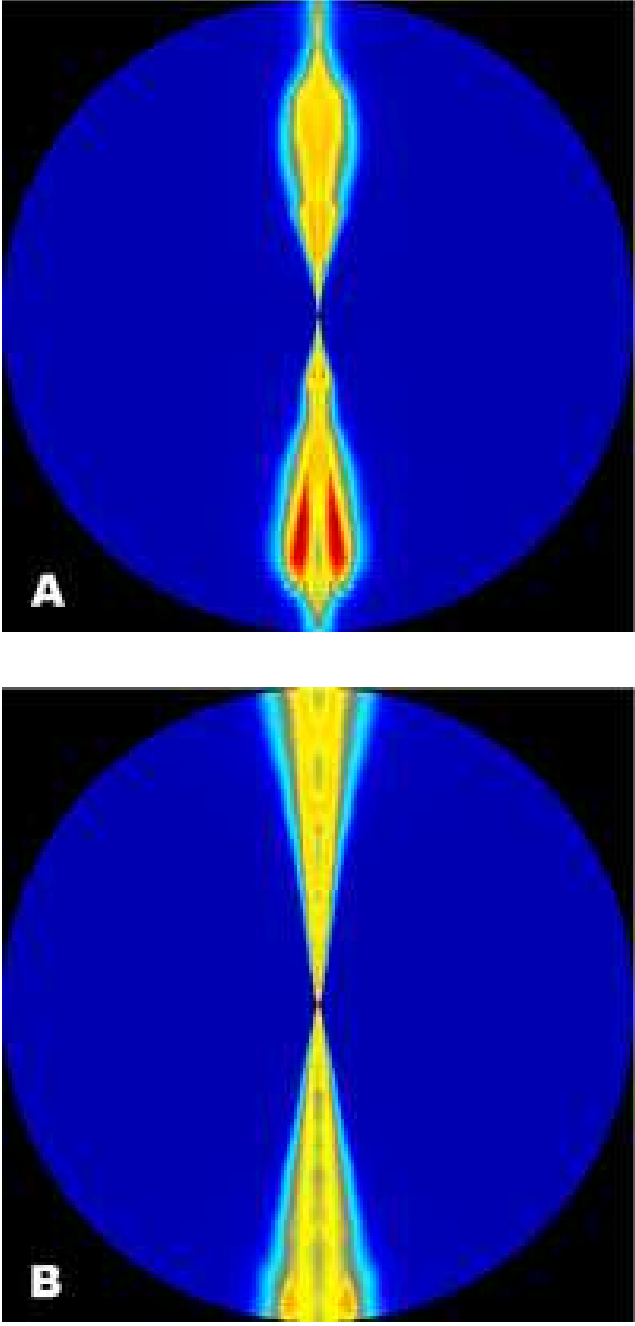


FIG. 8.—Jet becomes conical at large radii with a core half-opening angle $\theta_j \approx 5^\circ$. Plot of $\log \Gamma_\infty$ with red highest ($\Gamma_\infty \sim 10^4$) and blue lowest. Yellow is $\Gamma_\infty \sim 10^2 - 10^3$. Panel (A) has outer scale of $r = 10^4 GM/c^2$. Panel (B) outer scale $r = 10^3 GM/c^2$. Jet is independent of initial conditions by $r \approx 5 \times 10^3 r_g$.

gone an atypically strong magnetic pinch instability. Various realizations show that the upper polar axis behavior is typical, so this is studied in detail below. The strong hollow-cone structure of the lower jet is due to the strongest field being located at the interface between the jet and envelope, and this is related to the fact that the BZ-flux is $\propto \sin^2 \theta$, which vanishes identically along the polar axis. It is only the disk+corona that has truncated the energy extracted, otherwise the peak power would be at the equator.

Figure 9 shows the velocity structure of the Poynting-

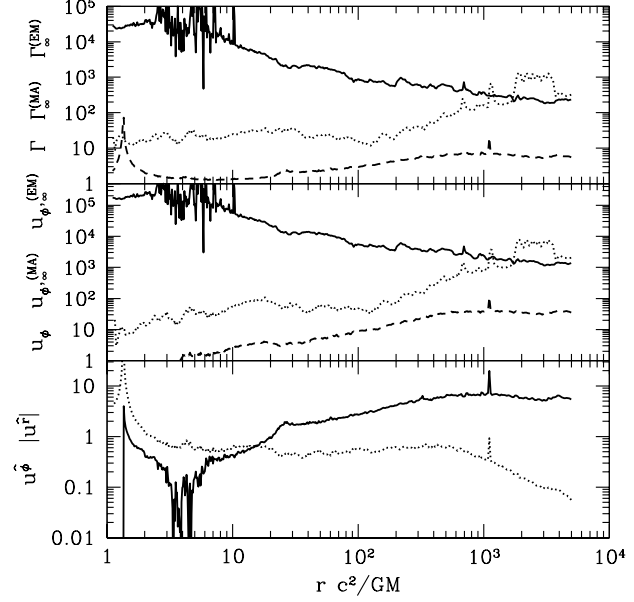


FIG. 9.—A radial cross section along a mid-level field of the jet showing the velocity structure. Top panel shows formation of magnetic fireball where matter (MA) and electromagnetic (EM) energy flux per unit rest-mass flux has $\Gamma_\infty^{(MA)} \sim \Gamma_\infty^{(EM)}$.

dominated jet along a mid-level field line. The top panel shows the late-time time-averaged values of $\Gamma_\infty^{(EM)}$ (solid line), $\Gamma_\infty^{(MA)}$ (dotted line), and $\Gamma = u^\hat{r} [\text{BL-coords}]$ (dashed line) as a function of radius along a mid-level field line. For $2 \lesssim r \lesssim 10$, the value of $\Gamma_\infty^{(EM)}$ is highly oscillatory. This shows the location of the stagnation surface, where the poloidal velocity $u^p = 0$, is temporally variable. The stagnation surface varies between $2 \lesssim r \lesssim 10$, within the range studied in prior sections. This is where ideal-MHD approximation is breaking and thus at any moment the value of $\Gamma_\infty^{(EM)}$ nearly diverges. Notice that while at $r \lesssim 10^3 r_g$ the Poynting flux dominates, the Poynting flux energy is slowly converted into enthalpy flux due to nonlinear time-dependent shock heating. Shocks are expected beyond the magneto-fast surface (see, e.g., Bogovalov & Tsinganos 2005) and here are due to pinch instabilities (Eichler 1993; Begelman 1998). For $r \gtrsim 10^3 r_g$, the enthalpy flux and Poynting flux are in equipartition.

Thus a “magnetic fireball” has developed and the terminal Lorentz factor is of order $\Gamma_\infty \sim 400$ for this choice of flow line. The Lorentz factor by $r \sim 10^4$ is still only $5 \lesssim \Gamma \lesssim 10$, with smaller patches with $\Gamma \sim 25$. This implies there will be an extended acceleration region where the magnetic fireball loses energy during adiabatic expansion. These results should also help motivate the boundary conditions used in jet simulations (Aloy et al. 2000; Zhang, Woosley, & MacFadyen 2003; Zhang W. et al. 2004), which sometimes start out with $\Gamma \sim 50$ and $u/\rho_0 \sim 150$ near the black hole. Such a high enthalpy only occurs by $10^3 r_g$ in our simulations. Their simulations are somewhat indicative of the Lorentz factor growth beyond our simulated time and radial range. This suggests that $\Gamma \sim 100$ should occur by $r \sim 10^6 r_g$ and that $\Gamma \sim 10^3$ should occur by $r \sim 10^7 r_g$. This is sufficient to avoid the compactness problem. A simulation of the acceleration region is left for future work.

The next lower panel of figure 9 shows the electromagnetic contribution to the specific angular momentum at infinity ($L = \Phi B_\phi$) (solid line), the matter contribution to the spe-

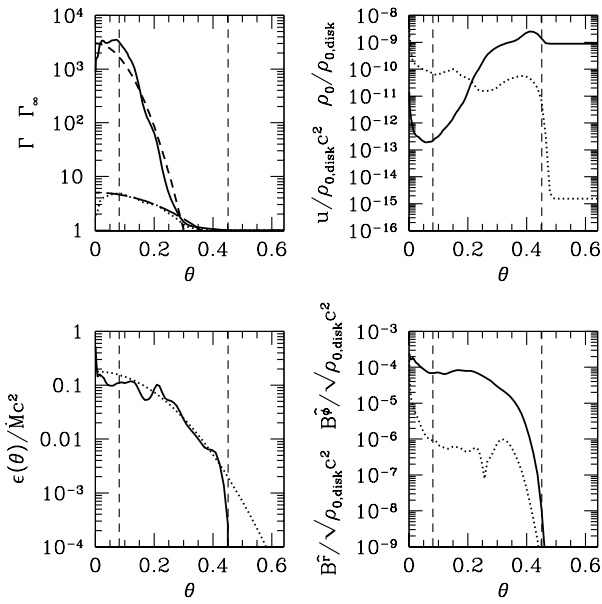


FIG. 10.— A θ cross-section of the jet at $r = 5 \times 10^3 GM/c^2$ showing the velocity, density, energy, and magnetic structure in Gauss. Velocity and energy structure show Gaussian fits as dashed lines. Vertical dashed lines marks outer and core jet.

cific angular momentum at infinity (hu_ϕ) (dotted line), and the specific angular momentum u_ϕ (dashed line).

The bottom panel of figure 9 shows the orthonormal radial ($u^r = \sqrt{g_{rr}}u^r$) (solid line) and ϕ ($u^\phi = \sqrt{g_{\phi\phi}}u^\phi$) (dotted line) 4-velocities in Boyer-Lindquist coordinates. The directed motion becomes relativistic, while the ϕ -component of the 4-velocity becomes sub-relativistic. However, the rotation is still large enough that it may stabilize the jet against $m = 1$ kink instabilities, as shown in the nonrelativistic case (Nakamura & Meier 2004).

Figure 10 shows the θ cross-section of the jet at $r = 5 \times 10^3 r_g$ for the upper polar axis according to figures 3, 4, and 8. This is a location by which the jet has stabilized in time, where farther regions are still dependent on the initial conditions. The hot fast “core” of the jet includes $\theta \lesssim 5^\circ$ at this radius and is marked by the left dashed vertical line. Also, it is useful to notice that $\theta \approx 0.14$ corresponds to the radius obtained for the “mid-level” field line shown for radial cross-sections in figures 9 and 11.

The region within $\theta \lesssim 27^\circ$ is an expanded cold slow portion of the jet. It is possible that the gamma-ray burst photons are due to Compton drag from soft photons emitted by this jet “sheath” dumping into the faster spine (Begelman & Sikora 1987; Ghisellini et al. 2000; Lazzati et al. 2004). Based upon the data fits described below for $r \gtrsim 120r_g$ and a radiation-dominated plasma, the outer sheath’s ($\theta \approx 0.2$) seed photon temperature as a function of radius is

$$T_{\gamma,seed} \sim 50\text{keV} \left(\frac{r}{5 \times 10^3 r_g} \right)^{-1/3} \quad (9)$$

These seed photons can be upscattered by the jet and produce a GRB and high energy components. A self-consistent study of a Compton dragged jet that determines Γ and the emission energy is left for future work.

The right dashed vertical line marks the boundary between the last field line that connects to the black hole. Beyond this region is the surrounding infalling medium. The upper-left

panel shows Γ_∞ (solid line), Γ (dotted line) and Gaussian fits to these two as dashed and long-dashed overlapping lines. The lower left panel shows the angular energy structure of the jet where $\epsilon(\theta) \equiv -r^2 T_t^r \approx r^2 \rho_0 u^r \Gamma_\infty$ with an overlapping Gaussian fit as a dotted line. The right panels show the density and magnetic structure of the jet. The upper right panel shows the density (solid line) and internal energy density (dotted line). The lower right panel shows the orthonormal Boyer-Lindquist coordinate toroidal (solid line) and radial (dotted line) field components.

This jet structure is weakly due to an interaction with the surrounding medium, and primarily due to internal evolution of the jet. Clearly the slower jet envelope is non-negligible, giving credence to the universal structured jet (USJ) model, but see Lamb et al. (2004) and see Zhang B. et al. (2004); Lloyd-Ronning et al. (2004). Gaussian jets have been used to explain a universal connection between GRBs and x-ray flashes (Zhang B. et al. 2004). In most of our simulated models the jet structure is Gaussian with $\epsilon(\theta) = \epsilon_0 e^{-\theta^2/2\theta_0^2}$, where $\epsilon_0 \approx 0.18$ and $\theta_0 \approx 8^\circ$, within the range that they suggest fits observations. The total luminosity per pole is $L_j \approx 0.023 \dot{M}_j c^2$, where 10% of that is in the “core” peak Lorentz factor region of the jet within a half-opening angle of 5° . Also, Γ_∞ is approximately Gaussian with $\Gamma_{\infty,0} \approx 3 \times 10^3$ and $\theta_0 \approx 4.3^\circ$. Also, Γ is approximately Gaussian with $\Gamma_0 \approx 5$ and $\theta_0 \approx 11^\circ$. This can be folded into various models, such as the probability of observing polarised emission in Compton drag emission models (Ghisellini et al. 2000; Lazzati et al. 2004).

For the collapsar model the above gives $L_j \approx 4 \times 10^{51} \text{erg s}^{-1}$ for this $j = 0.9375$ black hole model. This is approximately equal to the luminosity emitted by the black hole plus the energy in pairs produced by annihilating neutrinos. Not all of this energy can be observed in γ -rays to obtain $E_j \approx 2 \times 10^{51} \text{erg}$ for a 30 second event (Zhang B. et al. 2004), unless the black hole has spin $j \approx 0.6$ for most of the burst, which would suggest little spin evolution that requires a much thicker disk (Gammie, Shapiro, & McKinney 2004) and so less neutrino emission and annihilation efficiency. In McKinney (2005b), we found that Γ_∞ is weakly dependent on the black hole spin for $a \gtrsim 0.6$, so the Lorentz factor is likely unaffected by such changes.

It is more probable that the emission in γ -rays is inefficient or only a fraction of the total energy is observed (i.e. this requires $\lesssim 2\%$ for each if sole effect); or the true black hole mass accretion rate is lower than predicted by current collapsar models (i.e. $\dot{M}_0 \sim 0.002 M_\odot s^{-1}$ rather than $\dot{M}_0 \sim 0.1 M_\odot s^{-1}$ if sole effect). For the standard collapsar model, if one only observed the core of the jet, which has only 10% of the luminosity, then an efficiency of converting to γ -rays of $\approx 20\%$ is required to fit the model of Zhang B. et al. (2004).

Notice that the disk thickness (and so mass accretion rate) may strongly determine the collimation angle. In higher mass accretion rate systems, the disk is thicker than described here, and the final opening angle may be smaller. Also, if the mass accretion rate is much lower, the disk is also thicker (Kohri et al. 2005). The collapsar type model gives the thinnest disk near the black hole and small changes in the mass accretion rate lead to a small change in the disk thickness (Kohri et al. 2005). Also, for the relevant black hole spins, the spin only weakly determines the final collimation angle (McKinney & Gammie 2004). The universal jet model requires quite large opening angles that would not be supported by invoking stellar (and so black hole) spin depen-

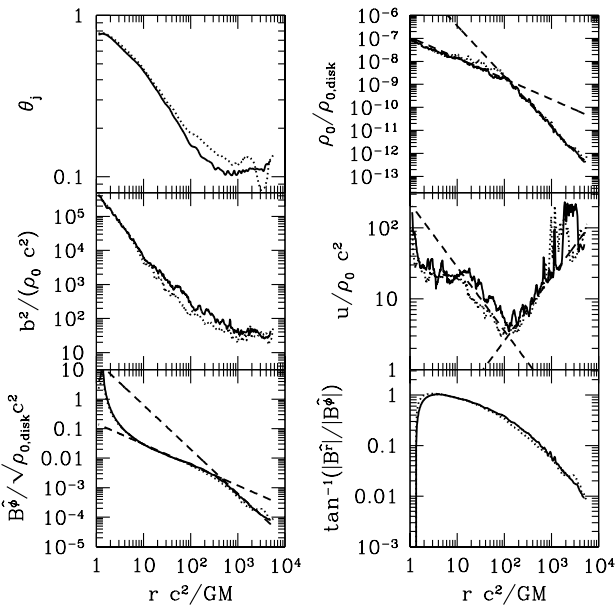


FIG. 11.— A radial cross-section of both poles of (solid and dotted lines) jet along a mid-level field line in the jet showing the jet collimation, density, and magnetic structure ($B^{\phi,r}$ in Gauss). Overlapping dashed lines are fits.

dence. It would also not be supported by invoking mass accretion rate dependence, since a system with a higher or lower accretion rate actually has a thicker disk (Kohri et al. 2005) and so stronger collimation.

There is a weak dependence on the density of the stellar envelope compared to that seen in relativistic hydrodynamic simulations of jets (Aloy et al. 2000; Zhang, Woosley, & MacFadyen 2003; Zhang W. et al. 2004), since here the confinement is mostly magnetic. During this energetic phase of the jet, the medium plays little role in shaping the core of the jet, as has been suggested for other reasons (Lazzati et al. 2005).

The peak Lorentz factors are obtained in a narrow region within a core with half-opening angle of $\theta \approx 5^\circ$. Notice as well that the very inner core of the jet is denser and slower, a feature predicted in the theoretical discussion of McKinney (2005b). This feature is simply a result that the Blandford-Znajek flux is $\propto \sin^2 \theta$. Most of the Poynting energy is initially at the interface between the jet and surrounding medium, until the jet internally evolves to collimate into a narrower inner core. Notice that in McKinney (2005b), we predicted $\Gamma_\infty \sim 1000$ for $j=0.9$, where the simulated results show a peak $\Gamma_\infty \approx 3 \times 10^3$ and typical $10^2 \lesssim \Gamma_\infty \lesssim 10^3$. This is in reasonable agreement with analytic estimates given the jet structure was not taken into account.

Figure 11 shows the collimation angle along a mid-level field line in the Poynting-dominated jet, along the same field line as in figure 9, and for both poles of the simulation. Generally the two poles are similar but not necessarily identical. Many simulations that were performed show at least one polar jet develop some pinch instabilities. In the model shown, one side develops very strong instabilities by the end of the simulation. The development of the pinch instability mostly affects the far-radial Lorentz factor (Γ and Γ_∞ — and so densities). The value of Γ is up to 5 times larger in pinched regions than non-pinched regions, while Γ_∞ can be up to a factor 10 times larger in pinched regions compared to non-pinched regions.

In figure 11, for $7r_g \lesssim r \lesssim 100r_g$ there is a region of col-

limation slightly faster than logarithmic. For the field line closest to the coronal wind (not shown) starting at $\theta_j \approx 1.0$, collimation is logarithmic with

$$\theta_j \approx 1 \left(\frac{r}{2.8r_g} \right)^{-1/3}. \quad (10)$$

Closer to the polar axis the collimation is faster. For the field line starting at $\theta_j \approx 0.3$, approximately

$$\theta_j \propto r^{-2/5} \quad (11)$$

up to $r \sim 10^2 r_g$. The inner-radial collimation is due to confinement by the disk+corona, while in the outer-radial range the coronal outflow collimates the Poynting flow. The corona is likely required for the Poynting-dominated jet collimation, since without a disk, a monopole-like field near the black hole actually decollimates at higher black hole spin (Krasnopolsky et al. 2005). Far from the coronal outflow, the internal jet is collimated by internal hoop stresses. Note that the classical hoop-stress paradigm that jets can self-collimate is not fully tested here, but these results suggest that collimation is in large part due to, or at least requires, the coronal outflow.

Notice from figure 9 that there is little acceleration beyond $r \sim 10^2 r_g$ while the magnetic fireball is forming. It is well known that magnetic acceleration requires field lines to collimate (Begelman & Li 1994). Once the flow is pseudo-conical the flow is unable to transfer magnetic energy into kinetic energy and proceeds to convert it into enthalpy flux. After $r \gtrsim 10^3 r_g$ the flow oscillates around a pseudo-conical asymptote with a mean half-opening angle of $\theta_j \sim 5^\circ$. The opening angle has been found to be weakly dependent on the black hole spin (McKinney & Gammie 2004) and, as found in this paper, the details of the injection model. This resulting pseudo-conical asymptote results once the magnetic energy no longer dominates and the coronal wind no longer helps collimate the flow. This opening angle is in line with expectations built around afterglow achromatic break measurements and estimates of the opening angle based upon energy of the burst. During the evolution of the burst, the jet may continue to collimate due to a more extended coronal outflow. This would be observed as an overall hard-to-soft evolution of γ -rays since one is gradually exposed to the slower edges of the jet since one likely does not observe exactly emission along the core center. The additional loading of neutrons from the coronal outflow may also lead to a hard-to-soft evolution of the jet as the overall Lorentz factor decreases over the duration of the burst.

Figure 11 shows the toroidal field and pitch angle, which shows that eventually the toroidal field completely dominates the poloidal field, and the toroidal field remains ordered. Thus, large polarizations up to 60% are possible (Granot & Königl 2003). The inner radial toroidal field is well fit by

$$\frac{B^\phi}{\sqrt{\rho_0, \text{disk} c^2}} [\text{Gauss}] = 0.0023 \left(\frac{r}{390r_g} \right)^{-0.7}. \quad (12)$$

The outer radial field is well fit by

$$\frac{B^\phi}{\sqrt{\rho_0, \text{disk} c^2}} [\text{Gauss}] = 0.0023 \left(\frac{r}{390r_g} \right)^{-1.5}. \quad (13)$$

The transition radius is $r \approx 390r_g$. Notice that this is along one mid-level field line, and the coefficients and power laws

are slightly different for each field line. The pitch angle shows that the field becomes toroidally dominated and at large radius the magnetic loops have a pitch angle of $\lesssim 1^\circ$ by $10^3 r_g$. For regions not on the axis there is no possibility of reconnection unless the flow is kink unstable (Drenkhahn 2002; Drenkhahn & Spruit 2002). Given the regularity of the flow field and the lack of randomized field, reconnection is *not* necessary or likely. Here, the pinch instability drives a nonlinear coupling such as shocks that converts the Poynting flux to enthalpy flux. This mechanism should be investigated in future work.

The toroidal field dominance leads to $m = 0$ pinch magnetic instabilities. The $m = 1$ kink mode may also operate, but studying the 3D jet structure is left for future work. As such oscillations develop, this leads to arbitrarily sized patches moving at arbitrary relative velocities as in the internal shock model. The typical size of a patch is $\sim 100 r_g$ to $\sim 10^3 r_g$ in the lab frame along the length of the jet. For long-duration GRBs lasting about 30 seconds, the number of pulses should be no larger than the ratio of the scale of the instability to the length of the event ($10^6 r_g$), or about 100–1000 pulses. Different realizations of the same simulation show that the likelihood of an instability growing is random, which could lead to the large variations in the number of observed pulses and explain the diversity of observed pulses (Nakar & Piran 2002). That is, some jets may have very few patches and so pulses. This type of instability is likely required to produce the diversity of GRBs. It is uncertain whether toroidal field instability induced variability dominates pair creation loading variability due to disk structure variability, which can be addressed by future work that self-consistently treats the neutrino emission from the disk.

Figure 11 also shows the rest-mass density per disk density, internal energy density per rest-mass density, and the ratio of (twice) the comoving magnetic energy density per unit rest-mass density. Notice that the density is close to that estimated in McKinney (2005b), so those calculations are likely reasonable approximations to the simulation results. The inner radial rest-mass density is well fit by

$$\frac{\rho_0}{\rho_{0,disk}} = 1.5 \times 10^{-9} \left(\frac{r}{120 r_g} \right)^{-0.9}. \quad (\text{inner}) \quad (14)$$

The outer radial rest-mass density is well fit by

$$\frac{\rho_0}{\rho_{0,disk} c^2} = 1.5 \times 10^{-9} \left(\frac{r}{120 r_g} \right)^{-2.2}. \quad (\text{outer}) \quad (15)$$

The transition radius is $r \approx 120 r_g$. Likewise, the inner radial internal energy density is moderately fit by

$$\frac{u}{\rho_{0,disk} c^2} = 4.5 \times 10^{-9} \left(\frac{r}{120 r_g} \right)^{-1.8}. \quad (\text{inner}) \quad (16)$$

The outer radial internal energy density is moderately fit by

$$\frac{u}{\rho_{0,disk} c^2} = 4.5 \times 10^{-9} \left(\frac{r}{120 r_g} \right)^{-1.3}. \quad (\text{outer}) \quad (17)$$

The transition radius is $r \approx 120 r_g$ and is due to the presence of the thick disk at small radii. Notice that this is along one mid-level field line, and the coefficients and power laws are slightly different for each field line. One can compare this to the “envelope” density model used with

$$\frac{\rho_0}{\rho_{0,disk}} = 8 \times 10^{-8} \left(\frac{r}{120 r_g} \right)^{-1.5}. \quad (\text{envelope}) \quad (18)$$

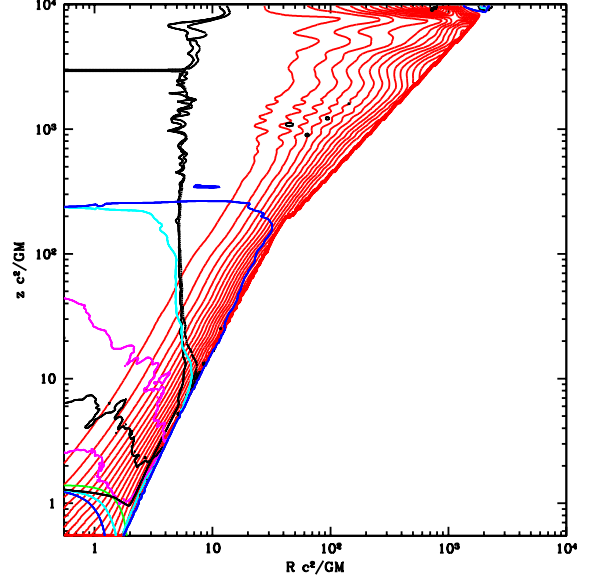


FIG. 12.— Jet becomes superfast and toroidal field dominates at large radii. Stagnation surface time-dependent but stable. Poynting-dominated jet characteristic (and other interesting) surfaces. Red lines are field lines. From $r = 0$ outwards: Blue#1: horizon + ingoing-fast ; Cyan#1: ingoing-Alfvén; Black#1: $B^\phi = B^\hat{r}$; Green#1: ergosphere ; Purple#1: ingoing-slow ; Black#2: stagnation surface where poloidal velocity $u^p = 0$; Purple#2: outgoing-slow ; Cyan#2: outgoing-Alfvén; Black#3: $B^\phi = B^\hat{r}$ again ; Black#4: light cylinder ; Blue#2: outgoing-fast.

The envelope has little impact on the jet structure.

Figure 12 shows the characteristic structure of the jet. The figure shows a log-log plot of one hemisphere of the time-averaged flow at late time. In such a log-log plot, 45° lines correspond to lines of constant θ . Lines of constant spherical polar r are horizontal near the z -axis and vertical near the R -axis. The field lines are shown as red lines. The disk and coronal regions have been truncated with a power-law cutoff for $r \lesssim 100 r_g$ and a conical cutoff for larger radii. The innermost blue line is the event horizon. Clearly the field lines are nearly logarithmic until $r \sim 100 r_g$. After this point the field lines stretch out and oscillate around a conical asymptote.

Blue lines in figure 12 show the ingoing and outgoing fast surfaces. Clearly the transition to a supercritical (superfast) flow has occurred. Within $r \lesssim 10 r_g$ the plotting cutoff creates the appearance that the fast surface and other lines terminate along the cutoff.

The inner magenta line is the ingoing slow surface, while the outer magenta line is the outgoing slow surface. The inner cyan line is the ingoing Alfvén surface. Energy can be extracted from the black hole if and only if the Alfvén surface lies inside the ergosphere (Takahashi et al. 1990). The ergosphere is shown by the green line, which is indeed outside the ingoing Alfvén surface. The outer cyan line is the outgoing Alfvén surface. The inner black line (next to the ergosphere) is the surface where $B^\phi = B^\hat{r}$ in Boyer-Lindquist coordinates. At larger radii there are two overlapping black lines. One corresponds to, again, where the toroidal field is equal to the poloidal field. The other corresponds to the light “cylinder” surface.

Other small artifacts in the plot are a result of unsteady nature of the flow. However, the despite the unsteady nature of the flow the characteristic structure is quite simple and rela-

tively smooth in appearance. This indicates that the flow is mostly stationary. The stagnation surface is fairly unsteady, but stable.

All the results discussed in this paper are robust to increases or decreases in numerical resolution. Convergence testing has been performed by choosing different models of the θ grid, including different Q_{jet} parameters that controls whether the disk or jet is more resolved at small radii. Another resolution of 256×256 instead of 512×256 was also chosen. No qualitative differences were found. The interpolation scheme was also changed from parabolic to linear and no qualitative differences for the far-field jet region were found.

We find that the pair injection model weakly determines the bulk structure of the flow at large radii. Other injection models were simulated by varying the total energy injected \dot{e}_{inj} , fraction of rest-mass created f_ρ , fraction of internal energy created f_h , fraction given to momentum energy f_m , and the ϕ -velocity of the injected particles. Only \dot{e}_{inj} and f_ρ strongly determine the bulk jet flow.

Most of these results are insensitive to the two different models of the surrounding medium. One model is a surrounding infall of material and the other is an “evacuated” exterior region. The jet structure is negligibly broader or narrower in the evacuated case due to magnetic confinement and collimation by the coronal outflow.

3.6. Simulation as Applied to AGN and X-ray Binaries

Notice that, quantitatively, all of these results can be simply rescaled by density in the jet in order to apply to other GRB models, AGN, and even approximately x-ray binary systems. This is because by the outer regions simulation, the jet has only reached about $\Gamma \sim 5-10$ and $\Gamma_\infty \propto 1/\rho_{0,jet}$.

In particular, numerical models for M87 give the same results with $2 \lesssim \Gamma \lesssim 10$ patches by $r \sim 10^3 r_g$. The key difference is that while the collapsar jet is very optically thick, the M87 jet is not so most of the shock-heated energy is lost to synchrotron radiation. The same structured jet is formed, and is useful to explain TeV BL Lac objects and radio galaxies (Ghisellini et al. 2005) and may help explain observations of blazars (Blandford & Levinson 1995; Ghisellini & Madau 1996; Chiaberge et al. 2000). The full opening angle of the jet core of $\sim 10^\circ$ also agrees with the observations of the far-field jet in M87 (Junor et al. 1999). As discussed previously, the shocks are synchrotron cooled and the heat generated does not contribute to larger scale acceleration. While self-consistent synchrotron cooling should be included, these results suggest the shock zone (or “blazar zone” for blazars) should be quite extended between $r \sim 10^2 r_g$ and up to about $r \sim 10^4 r_g$.

Similarly, simulations were performed using an injection model for GRS 1915+105 giving patches with $1.5 \lesssim \Gamma \lesssim 5$ by $r \sim 10^2 r_g$. Due to the efficient pair-loading there is little extra Poynting flux to convert to enthalpy flux or kinetic energy flux by the time shocks occur at $r \sim 10^2 r_g$. As discussed in McKinney (2005b), the Poynting-lepton jet in the GRS 1915+105 model is possibly destroyed by Compton drag by disk photons and synchrotron self-Compton and limited to at most $\Gamma \lesssim 2$, but the jet could be completely destroyed by Compton drag.

3.7. Summary of Fits

A summary of the fits along a fiducial field line is given. Near the black hole the half-opening angle of the full Poynting-dominated jet is $\theta_j \sim 1.0$, while by $r \sim 120 r_g$, $\theta_j \sim$

0.1. This can be roughly fit by

$$\theta_j \sim \left(\frac{r}{r_g} \right)^{-0.4} \text{ (inner)} \quad (19)$$

for $r < 120 r_g$ and $\theta_j \sim 0.14$ beyond. The core of the jet follows a slightly stronger collimation with

$$\theta_j \propto r^{-2/5} \quad (20)$$

up to $r < 120 r_g$ and $\theta_j \sim 0.09$ beyond. Also, roughly for M87 and the collapsar model, the core of the jet has

$$\Gamma_{bulk} \sim \left(\frac{r}{5r_g} \right)^{0.44} \text{ (inner)} \quad (21)$$

for $5 < r \lesssim 10^3 r_g$ and constant beyond for the M87 model if including synchrotron radiation, while the collapsar model should continue accelerating and the power law will truncate when most of the internal and Poynting energy is lost to kinetic energy and the jet becomes optically thin at about $r \sim 10^9 r_g$ or internal shocks take the energy away. If the acceleration is purely thermal without any magnetic effect, then $\Gamma \propto r$ (Mészáros & Rees 1997). However, it is not clear how the equipartition magnetic field affects the acceleration. Roughly for GRS 1915+105 the core of the jet has

$$\Gamma_{bulk} \sim \left(\frac{r}{5r_g} \right)^{0.14} \text{ (inner)} \quad (22)$$

for $5 < r \sim 10^3 r_g$ and constant beyond, with no account for Compton drag or pair annihilation. Also, for any jet system the base of the jet has $\rho_0 \propto r^{-0.9}$ (inner) for $r \lesssim 120 r_g$ and $\rho_0 \propto r^{-2.2}$ (outer) beyond. For the collapsar and M87 models

$$\frac{\rho_0}{\rho_{0,disk}} \sim 1.5 \times 10^{-9} \left(\frac{r}{120 r_g} \right)^{-0.9} \text{ (inner)} \quad (23)$$

and

$$\frac{\rho_0}{\rho_{0,disk}} \sim 1.5 \times 10^{-9} \left(\frac{r}{120 r_g} \right)^{-2.2} \text{ (outer)}, \quad (24)$$

while for GRS 1915+105 the inner-radial coefficient is 10^{-5} and outer is 6×10^{-3} . For the collapsar model, the inner radial internal energy density is moderately fit by

$$\frac{u}{\rho_{0,disk} c^2} = 4.5 \times 10^{-9} \left(\frac{r}{120 r_g} \right)^{-1.8} \text{ (inner)}. \quad (25)$$

The outer radial internal energy density is moderately fit by

$$\frac{u}{\rho_{0,disk} c^2} = 4.5 \times 10^{-9} \left(\frac{r}{120 r_g} \right)^{-1.3} \text{ (outer)}. \quad (26)$$

The transition radius is $r \approx 120 r_g$. For M87 the internal energy is near the rest-mass density times c^2 until $r \sim 120 r_g$ when the dependence is as for the collapsar case. For GRS 1915+105 the internal energy is near the rest-mass density times c^2 until $r \sim 120 r_g$ and then rises to about 2.5 times the rest-mass density times c^2 . The inner radial toroidal lab field is well fit by

$$\frac{B^\phi}{\sqrt{\rho_{0,disk} c^2}} [\text{Gauss}] = 0.0023 \left(\frac{r}{390 r_g} \right)^{-0.7} \text{ (inner)} \quad (27)$$

for $5 < r < 390 r_g$. The outer radial toroidal lab field is well fit by

$$\frac{B^\phi}{\sqrt{\rho_{0,disk} c^2}} [\text{Gauss}] = 0.0023 \left(\frac{r}{390 r_g} \right)^{-1.5} \text{ (outer)} \quad (28)$$

for $r > 390r_g$.

For the typical jet with no atypical pinch instabilities, the energy and velocity structure of the jet follow

$$\epsilon(\theta) = \epsilon_0 e^{-\theta^2/2\theta_0^2}, \quad (29)$$

where $\epsilon_0 \approx 0.18$ and $\theta_0 \approx 8^\circ$. The total luminosity per pole is $L_j \approx 0.023\dot{M}_0 c^2$, where 10% of that is in the “core” peak Lorentz factor region of the jet within a half-opening angle of 5° . Also, Γ_∞ is approximately Gaussian

$$\Gamma_\infty(\theta) = \Gamma_{\infty,0} e^{-\theta^2/2\theta_0^2}, \quad (30)$$

where $\Gamma_{\infty,0} \approx 3 \times 10^3$ and $\theta_0 \approx 4.3^\circ$. Also, Γ is approximately Gaussian

$$\Gamma(\theta) = \Gamma_0 e^{-\theta^2/2\theta_0^2}, \quad (31)$$

where $\Gamma_0 \approx 5$ and $\theta_0 \approx 11^\circ$. The outer sheath’s ($\theta \approx 0.2$) seed photon temperature as a function of radius is

$$T_{\gamma,seed} \sim 50\text{keV} \left(\frac{r}{5 \times 10^3 r_g} \right)^{-1/3}. \quad (32)$$

4. DISCUSSION

A collapsar-type GRMHD simulation with a neutrino annihilation model and Fick diffusion model has been studied. A self-consistent Poynting-dominated jet is produced and the Lorentz factor at large distances is $\Gamma_\infty \sim 10^3$ in the core of the jet, but an equally important structured component exists with $\Gamma_\infty \sim 10^2$. The Lorentz factor of the jet is determined by the electron-proton loading by Fick diffusion of neutrons. Notice that estimates of the baryonic mass-loading from the optical flash of GRB990123 suggest a baryon loading that gives $\Gamma \sim 10^3$ (Soderberg & Ramirez-Ruiz 2003), which is in basic agreement with the findings here. The half opening angle of the core of the jet is $\theta_j \sim 5^\circ$, while there exists a significant structured component with a half opening angle of $\theta_j \lesssim 25^\circ$. It is likely that this jet component survives traversing the remaining portion of the stellar envelope ($r \sim 10^5 r_g$, another decade in radius).

The jet at large distances is unstable to, at least, an $m = 0$ pinch instability due to the dominance of the toroidal field to the poloidal field (see, e.g. Begelman 1998). Here it is found that the energy of the jet is patchy. Typical realizations of the same model have a random number of patches with $100 \lesssim \Gamma_\infty \lesssim 10^3$. This likely results in a pulsed sequence of magnetic fireballs that move at large relative Lorentz factors, as required by the internal shock model (Mészáros 2002; Ghirlanda et al. 2003; Piran 2005). The acceleration region and internal shock region was not simulated since the dynamical range required is another ~ 6 orders of magnitude in radius.

Some models assume the Poynting energy to be converted into radiation far from the collapsing star by internal dissipation (see, e.g., Thompson 1994; Mészáros & Rees 1997; Spruit, Daigne, & Drenkhahn 2001; Drenkhahn 2002; Drenkhahn & Spruit 2002; Sikora et al. 2003; Lyutikov, Pariev, & Blandford 2003) such as magnetic reconnection. However, in our model, significant internal dissipation occurs already by $10^3 r_g$.

A very efficient model that reduces the compactness problem invokes Compton drag (bulk Comptonization) to generate the emission, where the stellar envelope or presupernova region provides soft photons (Ghisellini et al. 2000; Lazzati et al. 2004). Our numerical model shows a jet structure with a slow cold “sheath” necessary for supplying the

seed photons, so this process might explain the GRB emission process.

As in McKinney & Gammie (2004), a mildly relativistic Poynting-baryon jet is launched from the inner edge of the disk with a half-opening angle of roughly 16° to 45° , however long-time study of this jet component depends on sustaining long-time disk turbulence, which cannot be simulated in axisymmetry. For GRBs, this hot baryon-loaded jet might play a significant role in the subsequent supernova (by producing, e.g., ^{56}Ni) and be an interesting site for the r-process (Kohri et al. 2005). The mass ejection rate is found to be $\dot{M}_{0,coronal} \approx 0.03\dot{M}_0$, which for a 30 second event gives 0.1M_\odot of baryonic mass. This may be sufficient to power supernovae. The Lorentz factor is about $\Gamma \sim 1.5 - 3$, such as observed in a component of SN1998bw (Kulkarni et al. 1998).

For GRBs, the picture that emerges is that Poynting flux is emitted from the black hole at $r \sim r_g$ and is loaded with electron-positron pairs within $r \lesssim 20r_g$. A similar mass-fraction of neutrons Fick-diffuses into the jet, and they dominate the rest-mass once the temperature decreases to $T \lesssim 6 \times 10^9\text{K}$ by $r \sim 10r_g$. Magnetic acceleration occurs over $r \lesssim 10^2 r_g$ up to $\Gamma \sim 10$. Notice that this is in contrast to Mészáros & Rees (1997) who assumed the initial bulk Lorentz factor is $\Gamma[r = r_H] \sim \Gamma_\infty^{(EM)}$, which assumed instantaneous magnetic acceleration.

Once the toroidal field dominates the poloidal field, magnetic instabilities develops around $r \sim 10 - 10^2 r_g$ which turns the jet into an equipartition “magnetic fireball” by $r \sim 10^3 r_g$. The spatial structure of the magnetic fireball energy flux is patchy on the instability scale of $r \sim 10^2 r_g$. Simulations that demonstrate how these features would later interact require much more radial dynamic range. Between $10^4 r_g \lesssim r \lesssim 10^8 r_g$ the flow accelerates due to adiabatic expansion with a radial dependence up to $\Gamma \propto r$ (Mészáros & Rees 1997), where the Poynting flux provides a reservoir of magnetic energy that is continuously shock-converted into thermal energy.

After passing the stellar surface at $r \sim 10^5 r_g$, the plasma becomes transparent to γ -rays at $10^6 r_g \lesssim r \lesssim 10^7 r_g$, where possibly Compton drag of the sheath seed photons produces the GRB emission (Ghisellini et al. 2000; Lazzati et al. 2004). By $r \sim 10^7$, patches of varying $\Gamma \sim 100 - 1000$ have reached their terminal velocity. Between $10^8 r_g \lesssim r \lesssim 10^{10} r_g$ the fireball is optically thin to Compton scattering, radiation escapes, and pairs no longer annihilate but can continue to be magnetically accelerated (Mészáros & Rees 1997). Within this same radial range, internal shocks proceed to convert the remaining kinetic energy to nonthermal γ -rays. Beyond $10^{10} r_g$ a reverse shock may occur and external shocks with the interstellar medium (ISM) occur.

Simulations of AGN were performed, which show similar Γ vs. radius as the collapsar case. That is, there is an early transfer of Poynting flux to kinetic energy flux leading up to about $\Gamma \sim 5 - 10$ by about $r \sim 10^3 r_g$ for an M87 model. This is consistent with the lack of observed Comptonization features in blazars (see, e.g., Sikora et al. 2005), although this is also consistent with the fact that the optical depth to Comptonization is low in such systems.

While prior work assuming $\Gamma_{bulk} \sim 10$ and $\theta_j \sim 15^\circ$ found that the BZ power is insufficient to account for Blazar emission (Maraschi & Tavecchio 2003), as shown here the structure of the Poynting-dominated jet is nontrivial. The region with $\Gamma_{bulk} \sim 10$ is narrower with $\theta_j \sim 5^\circ$ and jet emission is likely dominated by shock accelerated electrons with

$\Gamma_e \gtrsim 100$ with an extended high energy tail. This lowers the necessary energy budget of the jet to be consistent with BZ power driving the jet.

4.1. Theoretical Contemporaneous Comparisons

Theoretical studies of ideal MHD jets focused on cold jets and the conversion of Poynting energy directly to kinetic energy (see, e.g., Li et al. 1992; Begelman & Li 1994; Daigne & Drenkhahn 2002). Indeed, much of the work has focused on self-similar models, of which the only self-consistent solution found is suggested to be R-self-similar models (Vlahakis 2004). Unfortunately, such models result in only cylindrical asymptotic solutions, which is apparently not what is observed in AGN jets nor present in the simulations discussed in this paper. The previous section showed that some aspects of the jet are nearly self-similar and that there is some classic ideal-MHD acceleration occurring in this region. However, once the toroidal field dominates the poloidal field, the Poynting flux is converted into internal energy until they reach equipartition. The conversion is due to a time-dependent nonlinear coupling, such as shocks, due to the magnetic pinch instability. Cold ideal-MHD jet models would have no way of addressing this. This region also involves relatively rapid variations in the flow, so stationary jet models would have difficulty modelling this region.

Notice that GRMHD numerical models show that the magnetic field corresponding to the Blandford-Znajek effect dominates all other magnetic field geometries (Hirose et al. 2004; McKinney 2005a). For example, there are no dynamically stable or important field lines that tie the black hole to the outer accretion disk as in Uzdensky (2005). All black hole field lines tie to large distances or tie to the horizon-crossing accretion disk. Also, there are no field lines that connect the inner-radial accretion disk and large distances. The Blandford-Znajek associated magnetic field is completely dominant, as shown in, e.g., figure 3 and figure 4.

We have not directly included those effects of neutron diffusion that induce a jet structure (Levinson & Eichler 2003). However, there is probably strong mixing within the jet and the large-scale jet is probably not affected by the details of the interface where neutron-diffusion occurs. Alternatively, the Gaussian structure we find may dominate the power law structure they find since the Gaussian structure is due to a strong internal electromagnetic evolution of the jet and matter plays little role in setting the jet structure.

4.2. Numerical Contemporaneous Comparisons

MacFadyen & Woosley (1999) evolve a presupernova core with a black hole inserted to replace part of the core and evolve the nonrelativistic viscous hydrodynamic equations of motion for various values of viscosity coefficient (α), mass accretion rate, nuclear burning, stellar angular momentum, and some models have an injected energy at the poles at some fixed energy rate. For models in which they inject energy at some specified rate, they find the baryon-contamination problem is somewhat alleviated by forming a hot bubble. As shown in their figure 28, they find the jet has $u/(\rho_0 c^2) \sim 10$ and they suggest that this corresponds to $\Gamma_\infty \sim 10$, insufficient to avoid the compactness problem. Their $\alpha = 0.1$ model shows a significant disk outflow, which over the duration of the GRB would yield $M \sim M_\odot$ in mass that could power a supernova. In their $\alpha = 0.01$ model there are insignificant outflows.

Our MHD results are most comparable to their $\alpha = 0.01$ model. We find a disk outflow yielding $M \sim 0.1 M_\odot$, which may still be sufficient to produce a supernova component. We have self-consistently evolved the jet formation and included an approximate model for the pair creation physics. In our case the baryon-contamination problem is self-consistently avoided by magnetic confinement of the jet against baryons, where only a small number of neutrons Fick-diffuse into the jet and self-consistently determine the Lorentz factor at large distances. We find that neutrino annihilation energy is probably dominated by energy from the black hole. Notice that we find $\Gamma_\infty \sim 100 - 1000$, which is much larger than they find. The difference between their and our model is the presence of a magnetic field and a rotating black hole, which drive the BZ-effect and a stronger evacuation of the polar jet region.

Proga (2005) have performed nonrelativistic MHD simulations of collapsars with a realistic equation of state. They suggest MHD accretion is able to launch, collimate, and sustain a strong Poynting outflow, although they measure a jet velocity of $v \sim 0.2c$. They find the jet is Poynting flux dominated such that $\Gamma_\infty \lesssim 10$, insufficient to avoid the compactness problem. The rotation of the black hole is crucial to generate a sufficiently Poynting-dominated jet. Similar fully relativistic simulations by Mizuno et al. (2004) have performed with a jet velocity of only $v \sim 0.3c$, which is due to their choice of the “floor” model in the polar regions and the short time of integration.

Zhang, Woosley, & MacFadyen (2003); Zhang W. et al. (2004) use a relativistic hydrodynamic model to simulate jet propagation through the stellar envelope and subsequent breakout through the stellar surface. They assume a highly relativistic jet is formed early near the black hole and they inject the matter with a large enthalpy per baryon of about $u/\rho_0 c^2 \sim 150$. They also tune the injected energy to compare with observations (Frail et al. 2001). In their view, variability is due to hydrodynamic instabilities between the cocoon and core of the jet. They find the stellar envelope can collimate the flow.

We have self-consistently evolved the *formation* of the jet along with the disk without having to assume a jet structure. We suggest that the injected energy per baryon is only $u/\rho_0 c^2 \lesssim 20$ unless super-efficient neutrino mechanisms are invoked. We also find that the self-consistent energy released is larger than observed, suggesting an fairly inefficient generation of γ -rays and a dominant lower Γ jet component that may explain x-ray flashes. We suggest magnetic instabilities due to pinch or kink modes dominate the variability rather than hydrodynamic instabilities, which are known to be quenched by magnetic confinement. We find that the jet structure is negligibly broader for models with no stellar envelope due to magnetic confinement and we find that the outer portion of the Poynting-dominated jet is collimated by the coronal outflow.

Many hydrodynamic jet propagation simulations have been studied (for a review see Scheck et al. 2002). Scheck et al. (2002) evolve hydrodynamic relativistic hadronic and leptonic jets using a realistic equation of state. They find that the resulting morphology of the jets are similar, despite the different composition. This suggests jet gross morphology is not a useful tool to differentiate jet composition. In our model, the most relativistic jet component is lepton-dominated in AGN and x-ray binaries and baryon-dominated in GRB systems. Notice that magnetic confinement quenches most hydrodynamic instabilities.

De Villiers et al. (2005b) evolve a fully relativistic, black

hole mass-invariant model, showing a jet with hot blobs moving with $\Gamma \sim 50$. A primary result in agreement with the results here is that a patchy or pulsed “magnetic fireball” is produced. This is gratifying since it suggests that the development of a “magnetic fireball” is not an artifact of the numerical implementation but is a likely result of shock heating. We also agree in finding that the core of the jet is hot and fast and is surrounded by a cold slow flow. One difference is that they say they seem to find the flow is cylindrically collimated by $r \gtrsim 300r_g$, while we find nearly logarithmic collimation until $r \sim 10^2r_g$ and an oscillatory conical asymptote beyond. Another difference is that they suggest temporal variability is due to injection events near the black hole, while we suggest it is due to pinch (or perhaps kink) instabilities at $r \gtrsim 10^2r_g$.

Another difference is that they find a larger value of Γ at smaller radius than we find. Indeed, one should wonder why their black hole mass-invariant model applies to only GRBs and not AGN or x-ray binaries. This is a result of their *much* lower “floor” density of $\rho_0 \sim 10^{-12}\rho_{0,disk}$, which is not consistent with self-consistent pair-loading or neutron diffusion loading. Also, because they use a constant density floor, the jet region at large radius must be additionally loaded with an arbitrary amount of rest-mass. The typical “floor” model adds rest-mass into the comoving frame, but this artificially loads the jet with extra mass moving at high Γ . We suggest that rather than the acceleration occurring within $r \lesssim 700r_g$ of their simulation, that acceleration occurs much farther away before the emitting region at $r \lesssim 10^9r_g$. In their $\Gamma \sim 50$ knots the gas has $10^3 \lesssim u/\rho_0c^2 \lesssim 10^6$. This implies that their actual terminal Lorentz factor is on the order of $10^5 \lesssim \Gamma_\infty \lesssim 10^7$, which would imply that the external shocks occur before internal shocks could occur.

Komissarov (2005) study the BZ process and MHD Penrose process. They found that the prior “jet” results of (Koide, Shibata, Kudoh, & Meier 2002), who evolve only for $t \sim 100t_g$, are only a transient phenomena associated with the initial conditions. They also suggest that there are serious problems for the MHD-driven model of jets since they do not find jets in their models except for contrived field geometries. However, this is potentially due to three effects. First, their outer radius is $r \sim 50r_g$, while here we study out to $r \sim 10^4r_g$. The magnetic acceleration only leads to a logarithmic increase in the velocity, so a large radial range is required to observe relativistic motion. Second, magnetic acceleration requires collimating field lines (Begelman & Li 1994), and a disk or disk wind is probably required to collimate the magnetic outflow (Okamoto 1999, 2000). The “disk” that forms in their models is relatively thin. Third, to avoid numerical errors, they limit their solution to $b^2/(\rho_0c^2) \lesssim 100$. Here we find that a self-consistent source of jet matter from pair creation and neutron diffusion leads to $b^2/(\rho_0c^2) \sim 10^5$ near the black hole. These three effects are probably why they find no relativistic jets.

4.3. Limitations

As has been pointed out by Komissarov (2005), nonconservative GRMHD schemes often overestimate the amount of thermal energy produced. All GRMHD numerical models suffer from some numerical error. Shock-conversion of magnetic energy to thermal energy is modelled by HARM in the perfect magnetic fluid approximation with total energy conserved exactly. However, our numerical model may overestimate the amount of magnetic dissipation in shocks, and so the

shocks may more slowly convert magnetic energy to thermal energy. If this dissipation was delayed until the γ -ray photosphere at $r \sim 10^7 - 10^8r_g$, then those shocks could be directly responsible for the γ -ray emission from GRBs. Clarification of this issue is left for future work. However, we expect that toroidal field instabilities drive efficient magnetic dissipation as shown in the numerical results presented here.

In order to evolve for a longer time than simulated in this paper, other physics must be included. For long-term evolution of a GRB model, one must include disk neutrino cooling, photodisintegration of nuclei, and a realistic equation of state. If one wishes to track nuclear species evolution, a nuclear burning reactions network is required. For the neutrino optically thick region of the disk, radiative transport should be included. The self-gravity of the star should be included to evolve the core-collapse. This includes a numerical relativity study of the collapse of a rotating magnetized massive star into a black hole (see review by Stergioulas 2003, §4.3). The jet should be followed through the entire star and beyond penetration of the stellar surface (Aloy et al. 2000; Zhang, Woosley, & MacFadyen 2003; Zhang W. et al. 2004).

As applied to all black hole accretion systems, some other limitations of the numerical models presented include the assumption of axisymmetry, ideal MHD, and a non-radiative gas. The assumption of axisymmetry is likely not important for the inner jet region since our earlier results (McKinney & Gammie 2004) find quantitative agreement with 3D results (De Villiers, Hawley, & Krolik 2003). The primary observed limitation of axisymmetry appears to be the decay of turbulence (Cowling 1934), which we attempt to avoid by requiring a resolution that gives quasi-steady turbulence for much of the simulation. Also, the jet at large distances has already formed by the time turbulence decays, and by that time the jet at large radius is not in causal contact with the disk.

When the toroidal field dominates the poloidal field, eventually $m = 1$ kink instabilities and higher modes may appear (see, e.g., Nakamura et al. 2001; Nakamura & Meier 2004). Thus our models may underestimate the amount of oscillation in the flow and the conversion of Poynting flux to enthalpy flux.

The limitation of axisymmetry may also limit the efficiency of the Blandford-Znajek process. The magnetic arrested disk (MAD) model suggests that any accretion flow likely accumulates a large amount of magnetic flux near the black hole. This means the efficiency of extracting energy would be higher (Igumenshchev et al. 2003; Narayan et al. 2003).

We have neglected low-energy jet and disk radiative processes in the numerical simulations. Future work should include a model of synchrotron radiation for an AGN model in order to simulate the “jet” emission to verify the claims made in McKinney (2005b) that the broad “jet” emission observed by Junor et al. (1999) is actually the coronal outflow rather than the Poynting-dominated jet.

Also for AGN, a self-consistent simulation with synchrotron emission would likely show the continuous loss of Poynting flux until the synchrotron cooling timescale is longer than the jet propagation timescale, which still suggests the jet Poynting flux is finally in equipartition with the enthalpy flux. This would suggest that the shock-zone, and so emission region, is more extended ($r \sim 10^2 - 10^4r_g$) than the simulated shock-zone ($r \sim 10^2 - 10^3r_g$).

For AGN and x-ray binaries, the radiatively inefficient disk

approximation, which assumes electrons couple weakly to ions, may not hold. If the electrons and ions eventually couple near the black hole, then the disk might collapse into an unstable magnetically dominated accretion disk (MDAF) (Meier 2005). Like the MAD model, this might drastically alter the results here, although it is uncertain whether jets are actually produced under the conditions specified by the MDAD model.

The single-fluid, ideal MHD approximation breaks down under various conditions, such as during the quiescent output of x-ray black hole binaries, where a two-temperature plasma likely forms near the black hole as ions and electrons decouple (see, e.g., Narayan & Yi 1995). Resistivity plays a role in current sheets where reconnection events may generate flares as on the sun, such as possibly observed in Sgr A (Genzel et al. 2003). Finally, radiative effects may introduce dynamically important instabilities in the accretion disk (e.g. Gammie 1998; Blaes & Socrates 2003).

5. CONCLUSIONS

Primarily two types of relativistic jets form in black hole (and perhaps neutron star) systems. The Poynting-dominated jet region is composed of field lines that connect the rotating black hole to large distances. Since the ideal MHD approximation holds very well, the only matter that can cross the field lines are neutral particles, such as neutrinos, photons, and free neutrons.

In McKinney (2005b), we showed that the primary differences between GRBs, AGN, and black hole x-ray binaries is the pair-loading of the Poynting-dominated jet, a similar mass-loading by free neutrons in GRB-type systems, the optical depth of the jet, and the synchrotron cooling timescale of the jet.

In McKinney (2005b), we showed that for GRB-type systems the neutron diffusion flux is sufficiently large to be dynamically important, but small enough to allow $\Gamma \sim 100 - 1000$. Beyond $r \sim 10r_g$ many of the electron-positron pairs annihilate, so the Poynting-dominated jet is dominated in mass by electron-proton pairs from collision-induced neutron decay. Most of the energy is provided by the BZ effect instead of neutrino-annihilation.

In McKinney (2005b), we showed that for AGN and x-ray binaries, the density of electron-positron pairs established near the black hole primarily determines the Lorentz factor at large distances. Radiatively inefficient AGN, such as M87, achieve $2 \lesssim \Gamma_\infty \lesssim 10$ and are synchrotron cooling limited. The lower the γ -ray radiative efficiency of the disk, the more energy per particle is available in the shock-zone. Radiatively efficient systems such as GRS1915+105 likely have no Poynting-lepton jet due to strong pair-loading and destruction by Comptonization by the plentiful soft photons for x-ray binaries with optically thick jets. However, all these systems have a mildly relativistic, baryon-loaded jet when in the hard-low state when the disk is geometrically thick, which can explain jets in most x-ray binary systems.

A GRMHD code, HARM, with pair creation physics was used to evolve many black hole accretion disk models. The basic theoretical predictions made in McKinney (2005b) that determine the Lorentz factor of the jet were numerically confirmed. However, Poynting flux is not necessarily directly converted into kinetic energy, but rather Poynting flux is first converted into enthalpy flux into a “magnetic fireball” due to shock heating. Thus, at large distances the acceleration is primarily thermal, but most of that thermal energy is provided by shock-conversion of magnetic energy. In GRB systems

this magnetic fireball leads to thermal acceleration over an extended radial range. The jets in AGN and x-ray binaries release this energy as synchrotron and inverse Compton emission and so the jet undergoes negligible thermal acceleration beyond $r \sim 10^2 - 10^3 r_g$.

Based upon prior theoretical (McKinney 2005b) and this numerical work, basic conclusions for collapsars include:

1. Black hole energy, not neutrino energy, typically powers GRBs.
2. Poynting-dominated jets are mostly loaded by e^-e^+ pairs close to the black hole, and by e^-p pairs for $r \gtrsim 10r_g$.
3. BZ-power and neutron diffusion primarily determines Lorentz factor.
4. Variability is due to toroidal field instabilities.
5. Poynting flux is converted into enthalpy flux and leads to the formation of a “magnetic fireball.”
6. Patchy jet develops $10^2 \lesssim \Gamma_\infty \lesssim 10^3$, as required by internal shock model.
7. Random number of patches (< 1000 for 30 second burst) and so random number of pulses.
8. Energy structure of jet is Gaussian with $\theta_0 \approx 8^\circ$.
9. Core of jet with $\theta_j \approx 5^\circ$ can explain GRBs.
10. Extended slower jet component with $\theta_j \approx 25^\circ$ can explain x-ray flashes.
11. Coronal outflows with $\Gamma \sim 1.5$ may power supernovae (by producing, e.g., ^{56}Ni) with $M \sim 0.1\text{M}_\odot$ processed by corona.

Based upon prior theoretical (McKinney 2005b) and this numerical work, basic conclusions for AGN or x-ray binaries include:

1. Poynting-dominated jets e^-e^+ pair-loaded unless advect complicated field.
2. γ -ray radiative efficiency, and so pair-loading, determines maximum possible Lorentz factor.
3. Poynting-lepton jet is collimated with $\theta_j \approx 5^\circ$.
4. Extended slow jet component with $\theta_j \lesssim 25^\circ$.
5. For fixed accretion rate, variability is due to toroidal field instabilities.
6. Poynting flux is shock-converted into enthalpy flux.
7. In some AGN, shock heat in transonic transition lost to synchrotron emission and limits achievable Lorentz factor to $2 \lesssim \Gamma \lesssim 10$ (e.g. in M87).
8. Coronal outflows produce broad inner-radial jet features in AGN together with well-collimated jet component (e.g. in M87).
9. In some x-ray binaries, Compton drag loads Poynting-lepton jets and limits Poynting-lepton jet to $\Gamma \lesssim 2$ or jet destroyed.

10. In some x-ray binaries, Poynting-lepton jet optically thick and emits self-absorbed synchrotron.
11. Coronal outflows have collimated edge with $\Gamma \lesssim 1.5$.
12. Coronal outflows may explain all mildly relativistic and nonrelativistic jets in radiatively efficient systems (most x-ray binaries).

For AGN and X-ray binaries, the coronal outflow collimation angle is strongly determined by the disk thickness. The above conclusions regarding the collimation angle assumed $H/R \sim 0.2$ near the black hole and $H/R \sim 0.6$ far from the black hole, while $H/R \sim 0.9$ (ADAF-like) is perhaps more appropriate

for some systems. The sensitivity of these results to H/R is left for future work.

ACKNOWLEDGMENTS

I thank Avery Broderick for an uncountable number of inspiring conversations. I also thank Charles Gammie, Brian Punsly, Amir Levinson, and Ramesh Narayan, with whom each I have had inspiring conversations. I thank Scott Noble for providing his highly efficient and accurate primitive variable solver. I thank Xiaoyue Guan for providing her implementation of parabolic interpolation. This research was supported by NASA-ATP grant NAG-10780 and an ITC fellowship.

APPENDIX

A. GRMHD EQUATIONS OF MOTION WITH PAIR CREATION

A single-component GRMHD approximation that accounts for baryon conservation is summarized. Leptons are assumed to be conserved in the equation of state (EOS) and by accounting for free-streaming neutrinos. We assume an ideal gas EOS of relativistic particles and neglect radiative transport since we assume all particles either stream freely or are trapped in the fluid. Alternatively, we assume the initial conditions well-model the steady-state radiative equilibrium. We model the streaming photon/neutrino-annihilation into pairs by injecting rest-mass and energy-momentum at an appropriate fraction of the baryon density.

The black hole has a Kerr metric written in Kerr-Schild coordinates, where the Kerr metric in Kerr-Schild coordinates and the Jacobian transformation to Boyer-Lindquist coordinates is given in McKinney & Gammie (2004). We use Kerr-Schild rather than Boyer-Lindquist because in Kerr-Schild coordinates the inner-radial boundary can be placed inside the horizon and so out of causal contact with the flow. It is difficult to avoid interactions between the numerical inner boundary and the jet when using Boyer-Lindquist coordinates. This interaction leads to excessive variability in the jet since the ingoing superfast transition is not on the grid and then the details of the boundary condition significantly impact the jet. Numerical models of viscous flows have historically had similar issues (see, e.g., McKinney & Gammie 2002).

A single-component MHD approximation is assumed such that baryon number is conserved up to a source term due to pair creation due to either radiative annihilation or neutron diffusion, such that

$$(\rho_0 u^\mu)_{;\mu} = S_\rho, \quad (A1)$$

where $\rho_0 \equiv m_b n_b$, $m_b \approx m_n$ the neutron mass, $n_b = n_n + n_p$, and m_p is the proton mass. One may choose an arbitrary mass weight to define ρ_0 in the single component fluid approximation.

For a magnetized plasma the conservation of energy-momentum equations are

$$T^{\mu\nu}_{;\nu} = (T_{\text{MA}}^{\mu\nu} + T_{\text{EM}}^{\mu\nu})_{;\nu} = S_T^\mu. \quad (A2)$$

where $T^{\mu\nu}$ is the stress-energy tensor, which can be split into a matter (MA) and electromagnetic (EM) part. In the fluid approximation

$$T_{\text{MA}}^{\mu\nu} = (\rho_0 + u_g) u^\mu u^\nu + p_g P^{\mu\nu}, \quad (A3)$$

with a relativistic ideal gas pressure $p_g = (\gamma - 1)u_g$, $\gamma = 4/3$, and $P^{\mu\nu} = g^{\mu\nu} + u^\mu u^\nu$ is the projection tensor. Either $\gamma = 5/3$ or $\gamma = 4/3$ for either the baryon-dominated component or lepton-dominated component does not change the results described in section 3.

A.1. Injection Physics

A detailed pair creation model would self-consistently determine the distribution of rest-mass and energy-momentum injected, which is left for future work. In this paper, the rough results of Popham et al. (1999); MacFadyen & Woosley (1999) are used to approximate the neutrino annihilation and pair creation. They determine the energy density creation rate in pairs as measured by an observer at infinity (\dot{e}_{inj}). A monoenergetic, monomomentum injection of rest-mass and energy-momentum is assumed. That is, for a Lorentz invariant particle distribution function of

$$f = \frac{dN}{dx^1 dx^2 dx^3 du^1 du^2 du^3}, \quad (A4)$$

the fluid equations are derived from the Boltzmann equation

$$\frac{df}{d\tau} = \frac{dn_{inj}}{d\tau} \delta[u^\mu - u_{inj}^\mu] \quad (A5)$$

for a particle creation density rate $dn_{inj}/d\tau$ in the comoving frame of the existing fluid. There is no collisional term in the ideal case. After mass-weighting and taking 4-velocity moments of the Boltzmann equation one has $S_\rho = (\rho_{0,inj} u_{inj}^\mu)_{;\mu}$, where $\rho_{0,inj}$ is the injected rest-mass density and u_{inj}^μ is the 4-velocity of the injected particles. Also, $S_T^\mu = T_{inj}^{\mu\nu} \delta_{;\nu}$. Here,

$$\frac{dn_{inj}}{d\tau} \equiv \frac{m_e}{m_b} \frac{dn_{e^-e^+,inj}}{d\tau} = \frac{1}{m_b} \frac{d\rho_{0,e^-e^+,inj}}{d\tau}, \quad (A6)$$

so the fluid is still treated as a single component with a single mass weight m_b . As discussed in McKinney (2005b), this is a good approximation since the late-time Poynting-dominated jet region is dominated by lepton mass while the remaining region is dominated by baryon mass. The simultaneous advected flux of injected energy is neglected, so then $S_{T_f} = \sqrt{-g} \dot{e}_{inj}$ is valid in Boyer-Lindquist, Kerr-Schild, or modified Kerr-Schild coordinates. This two-step approach (similar to operator splitting), where particles are injected and *then* advected with the normal fluid, is a good approximation for typical numerical integrations that use a multi-step timestep approach. This is also a good approximation because the injection region has a small 4-velocity beyond the stagnation surface. Also, the error in the injection approximations being made is larger than the error in neglecting the advection term. Thus

$$S_\rho = \partial/\partial t(\sqrt{-g} \rho_{0,inj} u_{inj}^t), \quad (\text{A7})$$

and

$$S_{T_\mu} = \partial/\partial t(\sqrt{-g}(q_{0,inj} u_{inj}^t u_\mu^{inj} + p_{inj} \delta_\mu^t)). \quad (\text{A8})$$

where $q_{0,inj} \equiv \rho_{0,inj} + u_{inj} + p_{inj}$. This represents the source of energy-momentum, such as photon and neutrino losses emitted and absorbed and the pairs created by annihilation of photons or neutrinos. This accounts for, in the guise of the MHD approximation, “non-local” transport of energy and momentum. The injected particles are a relativistic gas with $\gamma = 4/3$ such that $p_{inj} = (\gamma - 1)u_{inj}$.

Two approximate injection methods are used to treat the injected momentum. One assumes that the momentum injected is mostly aligned with the axis with $u_{inj}^\theta = 0$ and either $v_{inj}^\phi = 0$ or $v_{inj}^\phi = \Omega[R = r_{stag}]$ for some typical origin of the neutrinos r_{stag} . For the other, the particles are injected in the comoving frame of the existing fluid (i.e. $u_{inj}^\mu = u^\mu$). It turns out that these different approaches lead to qualitatively similar results for the solution beyond the region where injection is important ($r \gtrsim 6r_L$ in the jet). The total energy density injected (\dot{e}_{inj} as defined by an observer at infinity) is partitioned between rest-mass, enthalpy, and momentum energy. The fraction of rest-mass injected is defined as f_ρ and so

$$\partial/\partial t(\sqrt{-g} \rho_{0,inj} u_{inj}^t) = f_\rho \sqrt{-g} \dot{e}_{inj}. \quad (\text{A9})$$

The fraction of internal energy related injected energy is defined as f_h , and so

$$\partial/\partial t(\sqrt{-g}((u_{inj} + p_{inj}) u_{inj}^t u_t^{inj} + p_{inj})) = f_h \sqrt{-g} \dot{e}_{inj}. \quad (\text{A10})$$

The fraction of rest-mass plus momentum energy injected is defined as $f_\rho + f_m$, and so

$$\partial/\partial t(\sqrt{-g} \rho_{0,inj} u_{inj}^t u_t^{inj}) = (f_\rho + f_m) \sqrt{-g} \dot{e}_{inj}. \quad (\text{A11})$$

Here $f_\rho + f_h + f_m = 1$.

McKinney (2005b) defines \dot{e}_{inj} , which along with the injection fractions and $u^\mu u_\mu = -1$ completely define the injection process by allowing one to solve for ρ_{inj} , u_{inj} , u_t^{inj} , and u_t^{inj} for a fixed time interval dt . Radiative cooling effects are important for studying hundreds of dynamical times, but otherwise can be neglected if the initial model is consistent with the time-averaged radiative properties. Future work will refine the treatment of the pair creation process, considering the creation effects in the locally flat comoving frame, once a self-consistent model is available.

A.2. Pair Plasma Annihilation

The electron-positron pair plasma that forms may annihilate itself into a fireball if the pair annihilation rate is faster than the typical rate of the jet (c^3/GM) near the black hole. Also, if the pair annihilation timescale is shorter than the dynamical time, then pair annihilation would give a collisional term in the Boltzmann equation. From the pair annihilation rate given in McKinney (2005b), one finds that $t_{pa} \gg GM/c^3$ for AGN and marginally so for x-ray binaries. Thus, pairs mostly do not annihilate, and so formally the pair plasma that forms in the low-density funnel region is collisionless so that the Boltzmann equation should be solved directly. Plasma instabilities and relativistic collisionless shocks are implicitly assumed to keep the pairs in thermal equilibrium so the fluid approximation remains mostly valid, as is a good approximation for the solar wind (see, e.g. Feldman & Marsch 1997; Usmanov et al. 2000). This same approximation has to be invoked for the thick disk state in AGN and x-ray binaries, such as for the ADAF model (McKinney 2004). For regions that pair produce slower than the jet dynamical time, each pair-filled fluid element has a temperature distribution that gives an equation of state with $P = \rho_{0,e^-e^+} k_b T_e / m_e$ rather than $P = (11/12)aT^4$, where a is the radiation constant. So most of the particles have a Lorentz factor of $\Gamma_e \sim u / (\rho_{0,e^-e^+} c^2)$ and little of the internal energy injected is put into radiation. This also allows the use of a single-component approximation. A self-consistent Boltzmann transport solution is left for future work.

On the contrary for GRB systems, due to the relatively high density of pairs, the time scale for pair annihilation is $t_{pa} \ll GM/c^3$ along the entire length of the jet. Thus a pair fireball forms and the appropriate equation of state is that of an electron-positron-radiation fireball. Thus, formally the pair fireball rest-mass density is not independent of the pair fireball internal energy density. However, because the pairs are well-coupled to the radiation until a much larger radius of $r \sim 10^8 - 10^{10} r_L$, the radiation provides an inertial drag on the remaining pair plasma. That is, the relativistic fluid energy-momentum equation is still accurate. So the effective rest-mass density is $\sim \rho_0 + u$ (u the total internal energy of the fireball), and so the effective rest-mass is independent of the cooling of the fireball until the fireball is optically thin (see, e.g., Mészáros & Rees 1997).

For GRB systems, the mass conservation equation is reasonably accurate. Even though the electron-positron pairs annihilate, the rest-mass of pairs injected is approximately that of the pairs that are injected due to Fick-diffusion of neutrons (see appendix A of McKinney 2005b). The annihilation energy from electron-positron pairs contributes a negligible additional amount of internal energy, so can be neglected, especially compared to the Poynting energy flux that emerges from the black hole. Thus, the rest-mass can always be assumed to be due to baryons rather than the electron-positron pairs. This also suggests that the neutrino annihilation is a negligible effect if the BZ power is larger than the neutrino annihilation power.

In summary, the rest-mass evolution discussed in section 3 is accurate for GRB, AGN, and marginally so for x-ray binaries. This is despite the lack of Boltzmann transport for the collisional system, or a collisional term due to pair annihilation.

A.3. Electromagnetic Terms

In terms of $F^{\mu\nu}$, the Faraday (or electromagnetic field) tensor,

$$T_{\text{EM}}^{\mu\nu} = F^{\mu\gamma} F^{\nu\gamma} - \frac{1}{4} g^{\mu\nu} F^{\alpha\beta} F_{\alpha\beta}, \quad (\text{A12})$$

where a factor of $\sqrt{4\pi}$ is absorbed into the definition of $F^{\mu\nu}$. The induction equation is given by the space components of ${}^*F^{\mu\nu}_{;\nu} = 0$, where *F is the dual of the Faraday, and the time component gives the no-monopoles constraint. The other Maxwell equations, $J^\mu = F^{\mu\nu}_{;\nu}$, define the current density J^μ . The comoving electric field is defined as

$$e^\nu \equiv u_\mu F^{\mu\nu} = \frac{1}{2} \epsilon^{\mu\nu k\lambda} u_\nu {}^*F_{\lambda k} = \eta j^\nu, \quad (\text{A13})$$

where η corresponds to a scalar resistivity for a comoving current density $j^\mu = J_\nu P^{\nu\mu}$, where $P^{\nu\mu} \equiv g^{\nu\mu} + u^\nu u^\mu$ projects any 4-vector into the comoving frame (i.e. $P^{\nu\mu} u_\mu = 0$). The classical ideal MHD approximation that $\eta = e^\mu = 0$ is assumed. The comoving magnetic field is defined as

$$b^\nu \equiv u_\mu {}^*F^{\mu\nu} = \frac{1}{2} \epsilon^{\mu\nu k\lambda} u_\nu {}^*F_{\lambda k}, \quad (\text{A14})$$

and so the stress-energy tensor can be written as

$$T_{\text{EM}}^{\mu\nu} = \frac{b^2}{2} (u^\mu u^\nu + P^{\mu\nu}) - b^\mu b^\nu, \quad (\text{A15})$$

and

$${}^*F^{\mu\nu} = b^\mu u^\nu - b^\nu u^\mu \quad (\text{A16})$$

and so

$$F^{\mu\nu} = \epsilon^{\mu\nu\sigma\epsilon} u_\sigma b_\epsilon \quad (\text{A17})$$

since ${}^*F^{\mu\nu} = \frac{1}{2} \epsilon^{\mu\nu\kappa\lambda} F_{\kappa\lambda}$. Here ϵ is the Levi-Civita tensor. Following the notation of MTW, $\epsilon^{\mu\nu\lambda\delta} = -\frac{1}{\sqrt{g}} [\mu\nu\lambda\delta]$, where $[\mu\nu\lambda\delta]$ is the completely antisymmetric symbol and $= 0, 1$, or -1 . Notice that $e^\nu u_\nu = b^\nu u_\nu = 0$, so they each have only 3 independent components and are space-like 4-vectors.

With $B^i \equiv {}^*F^{it}$ and $E^i \equiv F^{it}$, the no-monopoles constraint becomes

$$(\sqrt{-g} B^i)_{,i} = 0, \quad (\text{A18})$$

and the magnetic induction equation becomes

$$(\sqrt{-g} B^i)_{,t} = -(\sqrt{-g} (b^i u^j - b^j u^i))_{,j}. \quad (\text{A19})$$

The ideal MHD approximation assumes that $e^\mu = 0$, and so the invariant $e^\mu b_\mu = 0$. Since the Lorentz acceleration on a particle is $f_l^\mu = qe^\mu$, then this implies that the Lorentz force vanishes on a *particle* in the ideal MHD approximation. Equation A14 implies $b^i = B^i u_i$ and $b^j = (B^i + u^i b^i)/u^t$, so the magnetic induction equation becomes

$$\begin{aligned} (\sqrt{-g} B^i)_{,t} &= -(\sqrt{-g} (B^i v^j - B^j v^i))_{,j} \\ &= -(\sqrt{-g} (\epsilon^{ijk} \varepsilon_k))_{,j}, \end{aligned} \quad (\text{A20})$$

where $v^i = u^i/u^t$, $\varepsilon_i = -\epsilon_{ijk} v^j B^k = -\mathbf{v} \times \mathbf{B}$ is the EMF, and ϵ^{ijk} is the spatial permutation tensor. A more complete account of the relativistic MHD equations can be found in Anile (1989).

B. CHARACTERISTIC (AND OTHER) SURFACES

The ideal MHD dispersion relation is given, e.g., in Gammie et al. (2003a) (there is a sign typo there), and summarized here. In the comoving frame, the dispersion relation is

$$\begin{aligned} D(k^\mu) &= 0 \\ \omega (\omega^2 - (\mathbf{k} \cdot \mathbf{v}_A)^2) \times & \\ (\omega^4 - \omega^2 (K_\mu^2 c_{ms}^2 + c_s^2 (\mathbf{k} \cdot \mathbf{v}_A)^2/c^2) + K^2 c_s^2 (\mathbf{k} \cdot \mathbf{v}_A)^2), & \end{aligned} \quad (\text{B1})$$

where $c_{ms}^2 = (\mathbf{v}_A^2 + c_s^2 (1 - \mathbf{v}_A^2/c^2))$ is the magnetosonic speed, $c_s^2 = (\partial(\rho+u)/\partial p)_s^{-1}$ is the relativistic sound speed, $\mathbf{v}_A = \mathbf{B}/\sqrt{\mathcal{E}}$ is the relativistic Alfvén velocity, $\mathcal{E} = b^2 + w$, and $w \equiv \rho + u + p$. Here c is the (temporarily reintroduced) speed of light. The invariant scalars defining the comoving dispersion relation are $\omega = k_\mu u^\mu$, $K^2 = K_\mu K^\mu = k_\mu k^\mu + \omega^2$, where $K_\mu = P_{\mu\nu} k^\nu = k_\mu + \omega u_\mu$ is the projected wave vector normal to the fluid 4-velocity, $\mathbf{v}_A^2 = b_\mu b^\mu/\mathcal{E}$, and $(\mathbf{k} \cdot \mathbf{v}_A) = k_\mu b^\mu/\sqrt{\mathcal{E}}$. The terms in the dispersion relation correspond to, respectively from left to right, the zero frequency entropy mode, the left and right going Alfvén modes, and the left and right going fast and slow modes. The eighth mode is eliminated by the no-monopoles constraint.

The dispersion relation gives the ingoing and outgoing slow, Alfvén, and fast surfaces. Energy can be extracted from the black hole if and only if the Alfvén point lies inside the ergosphere (Takahashi et al. 1990). Optimal acceleration of the flow by conversion of Poynting flux to kinetic energy flux occurs beyond the outer fast surface (Begelman & Li 1994). Other surfaces

include: the horizon at $r_H \equiv 1 + \sqrt{1 - j^2}$; the ergosphere at $r \equiv 1 + \sqrt{1 - (j \cos \theta)^2}$; the coordinate basis light surface in where $\sqrt{g_{\phi\phi}} = c/\Omega_F$, where asymptotically $\sqrt{g_{\phi\phi}} = r \sin(\theta)$ is the Minkowski cylindrical radius; the surface in Boyer-Lindquist coordinates where the toroidal field equals the poloidal field where $B^{\hat{\phi}} = B^{\hat{r}}$. Finally, there is a stagnation surface where the poloidal velocity $u^p = 0$. In a field confined jet where no matter can cross field lines into the jet, and if the jet has inflow near the black hole and outflow far from the black hole, then this necessarily marks at least one location where rest-mass must be created either by charge starving the magnetosphere till the Goldreich-Julian charge density is reached, or pair production rates sustains the rest-mass density.

REFERENCES

- Abramowicz, M., Jaroszinski, M., & Sikora, M. 1978, A&A, 63, 221
- Aloy, M. A., Muller, E., Ibanez, J. M., Marti, J. M., & MacFadyen, A. I. 2000, ApJ, 531, L119
- Anile, A. M. 1989, Relativistic Fluids and Magneto-fluids, (New York: Cambridge Univ. Press)
- Balbus, S. A. & Hawley, J. F. 1991, ApJ, 376, 214
- Begelman, M. C., & Sikora, M. 1987, ApJ, 322, 650
- Begelman, M. C., & Li, Z. 1994, ApJ, 426, 269
- Begelman, M. C. 1998, ApJ, 493, 291
- Blaes, O., & Socrates, A. 2003, ApJ, 596, 509
- Blandford, R. D., & Levinson, A. 1995, ApJ, 441, 79
- Bogovalov, S., & Tsinganos, K. 2005, MNRAS, 357, 918
- Chiaberge, M., Celotti, A., Capetti, A., & Ghisellini, G. 2000, A&A, 358, 104
- Colella, P., & Woodward, P. 1984, JCP, 54, 174
- Cowling, T. G. 1934, MNRAS, 94, 768
- Daigne, F., & Drenkhahn, G. 2002, A&A, 381, 1066
- De Villiers, J., Hawley, J. F., & Krolik, J. H. 2003, ApJ, 599, 1238
- De Villiers, J., Staff, J., & Ouyed, R. 2005, astro-ph/0502225
- Drenkhahn, G. 2002, A&A, 387, 714
- Drenkhahn, G. & Spruit, H. C. 2002, A&A, 391, 1141
- Eichler, D. 1993, ApJ, 419, 111
- Feldman, W. C., & Marsch, E.: 1997, in J. R. Jokipii, C. P. Sonett, and M. S. Giampapa (eds.), Cosmic Winds and the Heliosphere, Univ. of Arizona Press, Tucson, 617.
- Fender, R., & Belloni, T. 2004, ARA&A, 42, 317
- Fishbone, L.G., & Moncrief, V. 1976, ApJ, 207, 962
- Frail, D. A., et al. 2001, ApJ, 562, L55
- Gammie, C. F. 1998, MNRAS, 297, 929
- Gammie, C. F., McKinney, J. C., & Gábor Tóth 2003, ApJ, 589, 444
- Gammie, C. F., Shapiro, S. L., & McKinney, J. C. 2004, ApJ, 602, 312
- Gammie, C. F. 2004, ApJ, 614, 309
- Genzel, R., Schödel, R., Ott, T., Eckart, A., Alexander, T., Lacombe, F., Rouan, D., & Aschenbach, B. 2003, Nature, 425, 934
- Ghirlanda, G., Celotti, A., & Ghisellini, G. 2003, A&A, 406, 879
- Ghisellini, G., & Madau, P. 1996, MNRAS, 280, 67
- Ghisellini, G., Lazzati, D., Celotti, A., & Rees, M. J. 2000, MNRAS, 316, L45
- Ghisellini, G., & Celotti, A. 2002, Blazar Astrophysics with BeppoSAX and Other Observatories, 257
- Ghisellini, G. 2003, astro-ph/0310168
- Ghisellini, G., Tavecchio, F., & Chiaberge, M. 2005, A&A, 432, 401
- Granot, J. & Königl, A. 2003, ApJ, 594, L83
- Greiner, J., Cuby, J. G., & McCaughrean, M. J. 2001, Nature, 414, 522
- Hirose, S., Krolik, J. H., De Villiers, J., & Hawley, J. F. 2004, ApJ, 606, 1083
- Ho, L. C. 1999, ApJ, 516, 672
- Igumenshchev, I. V., Narayan, R., & Abramowicz, M. A. 2003, ApJ, 592, 1042
- Junor, W., Biretta, J. A., & Livio, M. 1999, Nature, 401, 891
- Kaiser, C. R., Gunn, K. F., Brocksopp, C., & Sokoloski, J. L. 2004, ApJ, 612, 332
- Kohri, K., & Mineshige, S. 2002, ApJ, 577, 311
- Kohri, K., Narayan, R., & Piran, T. 2005, astro-ph/0502470
- Koide, S., Shibata, K., Kudoh, T., & Meier, D. L. 2002, Science, 295, 1688
- Komissarov, S. S. 2005, MNRAS, 359, 801
- Krasnopolsky, R. et al., 2005, in prep.
- Kulkarni, S. R., et al. 1998, Nature, 395, 663
- Lamb, D. Q., Donaghy, T. Q., & Graziani, C. 2004, New Astronomy Review, 48, 459
- Lazzati, D., Rossi, E., Ghisellini, G., & Rees, M. J. 2004, MNRAS, 347, L1
- Lazzati, D., Begelman, M., Ghirlanda, G., Ghisellini, G., & Firmani, C. 2005, astro-ph/0503630
- Levinson, A., & Eichler, D. 2003, ApJ, 594, L19
- Levinson, A. 2005, astro-ph/0502346
- Li, Z., Chiueh, T., & Begelman, M. C. 1992, ApJ, 394, 459
- Lloyd-Ronning, N. M., Dai, X., & Zhang, B. 2004, ApJ, 601, 371
- Lyutikov, M., Pariev, V. I., & Blandford, R. D. 2003, ApJ, 597, 998
- MacFadyen, A. I., & Woosley, S. E. 1999, ApJ, 524, 262
- Maraschi, L., & Tavecchio, F. 2003, ApJ, 593, 667
- McKinney, J. C., & Gammie, C. F. 2002, ApJ, 573, 728
- McKinney, J. C. 2004, unpublished Ph.D. thesis, University of Illinois at Urbana-Champaign, <http://rainman.astro.uiuc.edu/~jon/research/thesis.pdf>
- McKinney, J. C., & Gammie, C. F. 2004, ApJ, 611, 977
- McKinney, J. C. 2005a, astro-ph/0506367
- McKinney, J. C. 2005b, astro-ph/0506368
- Meier, D. L. 2003, New Astronomy Review, 47, 667
- Meier, D. 2005, astro-ph/0504511
- Mészáros, P. 2002, ARA&A, 40, 137
- Mészáros, P., & Rees, M. J. 1997, ApJ, 482, L29
- Mirabel, I. F., & Rodriguez, L. F. 1994, Nature, 371, 46
- Mirabel, I. F., & Rodriguez, L. F. 1999, ARA&A, 37, 409
- Mizuno, Y., Yamada, S., Koide, S., & Shibata, K. 2004, ApJ, 615, 389
- Nakamura, M., Uchida, Y., & Hirose, S. 2001, New Astronomy, 6, 61
- Nakamura, M., & Meier, D. L. 2004, ApJ, 617, 123
- Nakar, E., & Piran, T. 2002, MNRAS, 331, 40
- Narayan, R., & Yi, I. 1995, ApJ, 452, 710
- Narayan, R., Igumenshchev, I. V., & Abramowicz, M. A. 2003, PASJ, 55, L69
- Noble, S.C. , Gammie, C.F., McKinney, J.C., Del Zanna, L.D., 2005, submitted.
- Okamoto, I. 1999, MNRAS, 307, 253
- Okamoto, I. 2000, MNRAS, 318, 250
- Shu, C.W. 1997, NASA/CR-97-206253, No.97-65
- Papaloizou, J. C. B., & Pringle, J. E. 1983, MNRAS, 202, 1181
- Phinney, E.S. 1983, unpublished Ph.D. thesis, Cambridge University
- Piran, T. 2005, Reviews of Modern Physics, 76, 1143
- Popham, R., Woosley, S. E., & Fryer, C. 1999, ApJ, 518, 356
- Proga, D. 2005, astro-ph/0502509
- Punsly, B. 1991, ApJ, 372, 424
- Reynolds, C. S., di Matteo, T., Fabian, A. C., Hwang, U., & Canizares, C. R. 1996, MNRAS, 283, L111
- Scheck, L., Aloy, M. A., Martí, J. M., Gómez, J. L., Müller, E. 2002, MNRAS, 331, 615
- Sikora, M., Begelman, M. C., Coppi, P., & Proga, D. 2003, ApJ, submitted, astro-ph/0309504
- Sikora, M., Begelman, M. C., Madejski, G. M., & Lasota, J. 2005, ApJ, 625, 72
- Soderberg, A. M., & Ramirez-Ruiz, E. 2003, AIP Conf. Proc. 662: Gamma-Ray Burst and Afterglow Astronomy 2001: A Workshop Celebrating the First Year of the HETE Mission, 662, 172
- Spruit, H. C., Daigne, F., & Drenkhahn, G. 2001, A&A, 369, 694
- Stergioulas, N. 2003, Living Reviews in Relativity, 6, 3
- Takahashi, M. , Nitta, S. , Tatematsu, Y. & Tomimatsu, A. 1990, ApJ, 363, 206
- Thompson, C. 1994, MNRAS, 270, 480
- Usmanov, A. V., Goldstein, M. L., Besser, B. P., & Fritzer, J. M. 2000, J. Geophys. Res., 105, 12675
- Uzdensky, D. A. 2005, ApJ, 620, 889
- Vlahakis, N. 2004, Ap&SS, 293, 67
- Woosley, S. E., & Weaver, T. A. 1995, ApJS, 101, 181
- Zhang, B., Dai, X., Lloyd-Ronning, N. M., & Mészáros, P. 2004, ApJ, 601, L119
- Zhang, W., Woosley, S. E., & MacFadyen, A. I. 2003, ApJ, 586, 356
- Zhang, W., Woosley, S. E., & Heger, A. 2004, ApJ, 608, 365
- Zhang, W., & MacFadyen, A. I. 2005, astro-ph/0505481